

Dear Dr. Juan Antonio Añel,

We hereby submit, for your consideration, the second revision of manuscript entitled “The Beijing Climate Center Climate System Model (BCC-CSM): Main Progress from CMIP5 to CMIP6”. We have incorporated all comments from two Referees in the revised manuscript. The point-to-point responses to Referees are enclosed in the following.

Thanks for considering this paper, and we look forward to hearing from you regarding its disposition.

Best regards,

Tongwen Wu, and all Co-Authors

*We thank both reviewers for their constructive and insight comments. We have carefully addressed these comments in the revised manuscript. All our responses are in Italic Font in the following point-to-point reply.*

## Response to Anonymous Referee #1

### General comments

The authors have addressed the issues from the review of the 1st version of their manuscript. In the following there are a number of comments and requests for clarification related to modified or new parts of the manuscript. Once these points are clarified and the manuscript is revised accordingly, I recommend its publication, so that this model documentation paper becomes available to the community.

### Detailed comments

L250... : "... In BCC-AGCM3-MR, the gravity wave drag generated from convective sources is introduced as in Beres et al. (2004), but drag by blocking effects is still not involved. ..." The Beres scheme parameterizes convective sources for the parameterized gravity wave drag. What about other sources, which may be important for the higher latitudes? Has the McFarlane scheme been tuned for the model simulations?

*Response: We have rewritten this paragraph and added more descriptions "Gravity waves generated by topography and fronts are important for higher latitudes. The efficiency parameter in the McFarlane scheme is set to 0.125 in BCC-AGCM2.2 and doubled to 0.25 in BCC-AGCM3-MR to obtain a better result of the polar night jet. In future, it is planned to improve the orographic gravity wave scheme and to implement parameterizations of gravity waves emitted by fronts and jets."*

L420: "... Figure 2 ... The whole system in BCC-CSM2-MR nearly reaches its equilibrium after 600 years. ..." "Thanks for adding Figure 2. You claim that the system has nearly reached an equilibrium after 600 years. But from Figure 2 one cannot distinguish, whether the system is still equilibrating, or the system has already equilibrated in combination with an energy leak/source of ca.  $+0.4\text{W/m}^2$ , or whether the equilibration is still ongoing in presence of a leak/source. What can be concluded from this figure is that the net TOA energy flux fluctuates without obvious trend around ca.  $0.4\text{ W/m}^2$ , while the SST of the 2nd 300 year period is a bit higher than in the 1st one. Additionally, I would like to ask the authors to display the global mean surface (or near surface) temperature, either in place of the SST or in addition. The main reason is that the Gregory plots (as in your Figure 6), which are relevant for judging "equilibration", relate the radiative forcing at TOA to the global mean surface temperature, not to SST.

*Response: We followed the suggestion and replaced SST by the global surface air temperature in Figure 2b. The corresponding paragraph was rephrased.*

L458-459: "... When a 9-year smoothing is applied ..." The caption of Figure 4 writes: "... of 11-year smoothed ..." Please clarify.

*Response: Thanks. We checked our script and the caption in Figure 4 is right. The filter uses 11 years.*

L466-467: "... There are two members (r1i1p1f1 and r2i1p1f1 in Fig. 4) of historical simulations of the CMIP6 model show a hiatus towards the end of the simulation that resembles the observed one ..." r3i1p1f1 is not comparable to the observed hiatus. This realization has a short spell of colder years centered at 2010, which is different to the lack of warming in the observational record and in r1i1p1f1 from ca. 2000 to the end of the simulations. Please modify your text.

*Response: We have reworded this sentence to make our point clearer. The revised text is "Although the third member (r3i1p1f1) simulated a global warming slowdown from 2004 to 2012, it is not comparable to the observed hiatus as it has a short spell of colder years centered at 2010."*

L472... : As you describe the earlier hiatus appears in r2, but not in r1, and the later hiatus occurs in r1, but not in r2. This clearly excludes any simple response to forcing, and makes internal variability a much more likely reason.

*Response: Thanks for your comments. We have rewritten this sentence as "So, the simulation of global warming hiatus in BCC CMIP6 model clearly excludes any simple response to forcing, and makes internal variability a much more likely reason"*

L485... : Figure 5 shows in most places between 60S and 60N a warm bias, so that the area average likely is also positive, i.e. the model is rather warmer than ERA-Interim. In Figure 4, however, the 60S to 60N average of the r1 simulation almost always is below the observed record, especially due to the strong response to the Mt. Pinatubo eruption. How does this fit together?

*Response: This is only a problem of reference. Figure 5 shows the surface air temperature as a difference to ERA-Interim during the same period of 1986 to 2005. But Figure 4 shows the anomalies of each dataset relative to its own climatology of 1961-1990.*

L528-529: Is the similarity of the ECS by chance, or was this a goal of the tuning procedure? Please clarify this in the manuscript.

*Response: This is entirely fortuitous. We added a phrase in the revised manuscript “We remind that this is a pure coincidence since we did not intentionally tune our model for its sensitivity”.*

L576... : “... The zonal mean of zonal wind biases in the high latitudes of the stratosphere in BCCCSM2-MR have increased near 10 hPa, where model biases may be partly caused by not yet involved gravity wave drag that generated by blocking effects. ... “ Blocking mainly affects the tropospheric circulation in regions of steep topography. The polar night jets are rather influenced by gravity wave drag. In any case, the too strong polar night jets indicate a too weak drag. Maybe some non-orographic gravity wave sources are not represented, see earlier comment.

*Response: We agree with this argument and have rewritten the corresponding paragraph as “The too-strong polar night jets clearly indicate an insufficient atmospheric drag at this level. It may be partly caused by the lack of effects in relation to some non-orographic gravity waves generated by atmospheric fronts and jets. We expect to reduce this model bias in next version by adding this process.”*

L596: “... which is possibly due to inadequate gravity wave forcing to drive the QBO. ... ” This is one possibility. But there is also the other one: The wave-meanflow interaction based on resolved waves (Kelvin waves, mixed Rossby-gravity waves, ... ) is probably not realistic. One reason that would contribute to such a deficiency is the relatively coarse vertical resolution that would affect the vertical wave lengths and the wave damping. (For the planned QBO-article: The separate analysis of resolved wave meanflow interaction and parameterized wind tendencies in the QBO domain, together with advective tendencies, will be important to understand the nature of the simulated QBO.)

*Response: We agree with your argument, and we hope that we will be able to improve QBO simulations by this approach.*

L633: “... the period ENSO periodicity ... “ → “... the mean period of ENSO ... “

*Response: Modified.*

## Response to Anonymous Referee #2

I am almost satisfied with the authors' revision. They have honestly responded to my comments. I have only minor comments as follows:

1. L74-75 "They differ only by their horizontal resolutions": The versions of the ocean and sea ice models are also different according to Table 1.

*Response: Thank you, the "only" should be replaced by "mainly".*

2. L544 and L608: Omit the bullet.

*Response: Modified.*

3. L584 "wind velocity at 850 hPa (U850 and V850) and at 200 hPa (U200)" >> "zonal and meridional wind velocity at 850 hPa (U850 and V850) and zonal wind velocity at 200hPa (U200)"

*Response: Modified.*

4. L587 "precipitation and zonal wind at 850 hPa" >> "PRCP and U850"

*Response: Modified.*

5. L589 "geopotential height at 500 hPa" >> "Z500"

*Response: Modified.*

6. L592 "precipitation" >> "PRCP"

*Response: Modified.*

7. L658-659 "cold SST in the eastern equatorial Pacific still extends too far west in both models and a cold tongue bias exists in the equatorial Pacific": It appears that the cold tongue cold bias is worse in BCC-CSM2-MR. Please touch on the issue.

*Response: Yes, this is a deterioration. We modified the revised manuscript as "However, cold SST in the eastern equatorial Pacific still extends too far west in both models and a cold tongue bias exists in the equatorial Pacific and even gets a little worse in BCC-CSM2-MR. The annual mean SST in the coldest center near 110 °W in the equatorial Pacific is below 23 °C in BCC-CSM2-MR, a deterioration compared to BCC-CSM1.1m."*

8. L670-671 "underestimated air-sea coupling strength": This is inconsistent with the fact that ENSO amplitude is overestimated in the models compared to the observation.

*Response: Please see next response.*

9. L672-673 "zonal advective feedback and thermocline feedback": It is known that the longer (4~5 year) ENSO period is related to the thermocline feedback rather than the zonal advection feedback (Guilyardi 2006).

Guilyardi, E., 2006: El Nino–mean state–seasonal cycle interactions in a multi-model ensemble. *Climate Dyn.*, 26, 329–348.

*Response: In terms of potential causes for the too-short periodicity of the ENSO cycle, we took the reference to the results of Lu and Ren (2016) which might be inconsistent with other researches. In order to avoid confusion, we deleted the phrases in question in the revised manuscript.*

10. Figure 13: The characteristic of ENSO irregularity is improved in BCC-CSM2-MR in comparison to BCC-CSM1.1m.

*Response: We have added “The characteristic of ENSO irregularity is improved in BCC-CSM2-MR in comparison to BCC-CSM1.1m”.*

11. Plots of sea-ice extent in Fig. 14 and 15 are still inconsistent each other. In Fig. 14a (the Arctic), BCC-CSM1.1m underestimates sea-ice extent compared to the Hadley data, although it overestimates in Fig. 15a (March). In the Antarctic, sea-ice extent simulated by BCC-CSM2-MR is too small in Fig. 14b, although the bias in Fig. 15b (March) is not so serious.

*Response: Thanks for your careful evaluation and checking. There were indeed inconsistencies in old Figs. 14 and 15, entirely due to our confusion in plotting figures and manipulating different data sources. In the revised manuscript, we have updated them, and also modified the corresponding text.*

12. L784-785 "The center of precipitation around Japan is also well simulated in BCC-CSM2-MR": Distribution of precipitation around Japan in Fig. 18 appears to be strange. The rain-band should develop during summer, while the simulated rain-bands active in winter.

*Response: This was partly induced by an inconsistency of color bars in Fig. 18 (summer versus winter). In order to avoid confusion, we replotted it using a same color bar.*

1 **The Beijing Climate Center Climate System Model (BCC-CSM): Main**  
2 **Progress from CMIP5 to CMIP6**

3  
4 **Tongwen Wu<sup>1\*</sup>, Yixiong Lu<sup>1</sup>, Yongjie Fang<sup>1</sup>, Xiaoge Xin<sup>1</sup>, Laurent Li<sup>1,2</sup>, Weiping Li<sup>1</sup>, Weihua Jie<sup>1</sup>,**  
5 **Jie Zhang<sup>1</sup>, Yiming Liu<sup>1</sup>, Li Zhang<sup>1</sup>, Fang Zhang<sup>1</sup>, Yanwu Zhang<sup>1</sup>, Fanghua Wu<sup>1</sup>, Jianglong Li<sup>1</sup>,**  
6 **Min Chu<sup>1</sup>, Zaizhi Wang<sup>1</sup>, Xueli Shi<sup>1</sup>, Xiangwen Liu<sup>1</sup>, Min Wei<sup>3</sup>, Anning Huang<sup>4</sup>, Yaocun Zhang<sup>4</sup>,**  
7 **Xiaohong Liu<sup>1,5</sup>**

8  
9 <sup>1</sup>Beijing Climate Center, China Meteorological Administration, Beijing, China

10 <sup>2</sup>Laboratoire de Météorologie Dynamique, IPSL, CNRS, Sorbonne Université Ecole Normale  
11 Supérieure, Ecole Polytechnique, Paris, France

12 <sup>3</sup>National Meteorological Information Center, China Meteorological Administration, Beijing, China

13 <sup>4</sup>Nanjing University, Nanjing, China

14 <sup>5</sup>University of Wyoming, Laramie, WY, United States

15  
16 *Correspondence to:* Tongwen Wu ([twwu@cma.gov.cn](mailto:twwu@cma.gov.cn))

17  
18 **(Revised on Feb. 10, 2019)**

19  
20 **Abstract.** Main progresses of Beijing Climate Center (BCC) climate system model from the phase five  
21 of the Coupled Model Intercomparison Project (CMIP5) to its phase six (CMIP6) are presented, in  
22 terms of physical parameterizations and model's performance. BCC-CSM1.1 and BCC-CSM1.1m are  
23 the two models involved in CMIP5. BCC-CSM2-MR, BCC-CSM2-HR, and BCC-ESM1.0 are the three  
24 models configured for CMIP6. Historical simulations from 1851 to 2014 from BCC-CSM2-MR  
25 (CMIP6) and from 1851 to 2005 from BCC-CSM1.1m (CMIP5) are used for models assessment. The  
26 evaluation matrices include (a) energy budget at top of the atmosphere, (b) surface air temperature,  
27 precipitation, and atmospheric circulation for global and East Asia regions, (c) sea surface temperature

28 | (SST) in the tropical Pacific, (d) sea ice extent and thickness and Atlantic Meridional Overturning  
29 Circulation (AMOC), and (e) climate variations at different time scales such as global warming trend in  
30 the 20<sup>th</sup> century, stratospheric quasi-biennial oscillation (QBO), Madden-Julian Oscillation (MJO) and  
31 diurnal cycle of precipitation. Compared to BCC-CSM1.1m, BCC-CSM2-MR shows significant  
32 improvements in many aspects including: tropospheric air temperature and circulation at global and  
33 regional scale in East Asia, climate variability at different time scales such as QBO, MJO, diurnal cycle  
34 of precipitation, interannual variations of SST in the equatorial Pacific, and long-term trend of surface  
35 air temperature.

36

## 37 **1. Introduction**

38 Changes of global climate and environment are main challenges that human societies are facing for  
39 sustainable developments. Climate and environment changes are often the consequence of combined  
40 effects of anthropogenic influences and complex interactions among the atmosphere, hydrosphere,  
41 lithosphere, cryosphere and biosphere of the Earth system. To better understand behaviors of the earth  
42 climate, and to predict its future evolution, appropriate new concepts and relevant methodologies should  
43 be proposed and developed. Climate system models are effective tools to simulate the interactions and  
44 feedbacks in an objective manner, and to explore their impacts on climate and climate change. The  
45 Coupled Model Intercomparison Project (CMIP) organized under the auspices of the World Climate  
46 Research Programme's (WCRP) Working Group on Coupled Modelling (WGCM) started twenty years  
47 ago as a comparison of a handful of early global coupled climate models (Meehl et al., 1997). More  
48 than 30 models participated in the phase five of CMIP (CMIP5, Taylor et al., 2012) and created an  
49 unprecedented dynamics in the scientific community to generate climate information and make them  
50 available for scientific researches. Many of these models were then extended into Earth System models  
51 by including the representation of biogeochemical cycles. BCC effectively contributed to CMIP5 by  
52 running most of the mandatory and optional simulations.

53 The first generation of Beijing Climate Center ocean-atmosphere Coupled Model BCC-CM1.0 was  
54 developed from 1995 to 2004 (e.g. Ding et al., 2002). It was mainly used for seasonal climate prediction.  
55 Since 2005, BCC initiated the development of a new fully-coupled climate modelling platform (Wu et

al., 2010, 2013, 2014). In 2012, two versions of the BCC model were released: BCC-CSM1.1 with a coarse horizontal resolution T42 (approximately 280 km) and BCC-CSM1.1m with a medium horizontal resolution T106 (approximately 110 km). It was a fully-coupled model with ocean, land surface, atmosphere, and sea-ice components (Wu et al., 2008; Wu, 2012; Xin et al., 2013). Both versions were extensively used for CMIP5. At the end of 2017, the second generation of the BCC model was released to run different simulations proposed by the phase six of CMIP (CMIP6, Eyring et al., 2016). The purpose of this paper is to document the main efforts and progress achieved in BCC for its climate model transition from CMIP5 to CMIP6. We show improvements in both model resolution and its physics. A relevant description on model transition, and experiment design are shown in Sections 2 and 3. A comparison of models performance is presented in Section 4. Conclusions and discussion are summarized in Section 5. Information about code and data availability is shown in Section 6.

## 2. Transition of the BCC climate system model from CMIP5 to CMIP6

Table 1 shows a summary of different BCC models or versions used for CMIP5 and CMIP6. All of them are fully-coupled global climate models with four components, atmosphere, ocean, land surface and sea-ice, interacting with each other. They are physically coupled through fluxes of momentum, energy, water at their interfaces. The coupling was realized with the flux coupler version 5 developed by the National Center for Atmosphere Research (NCAR). BCC-CSM1.1 and BCC-CSM1.1m are our two models involved in CMIP5. They differ mainly by their horizontal resolutions. As shown in Table 1, BCC-CSM2-MR, BCC-CSM2-HR, and BCC-ESM1.0 are the three models developed for CMIP6.

BCC-ESM1.0 is our Earth System configuration. It is a global fully-coupled climate-chemistry-carbon model, and intended to conduct simulations for the Aerosol Chemistry Model Intercomparison Project (AerChemMIP, Collins et al., 2017) and the Coupled Climate–Carbon Cycle Model Intercomparison Project (C4MIP, Jones et al., 2016), both endorsed by CMIP6. Its performance will be presented in a separated paper. BCC-CSM2-HR is our high-resolution configuration prepared for conducting simulations of the High Resolution Model Intercomparison Project (HighResMIP v1.0, Haarsma et al., 2016). It has 56 layers in the vertical, 0.092 hPa for the top of model. Its performance will also be presented separately.

84 In this paper, we focus on BCC-CSM1.1m and BCC-CSM2-MR. The two models are  
85 representative of our climate modelling efforts in CMIP5 and CMIP6 respectively. They have the same  
86 horizontal resolution (T106, about 110×110 km in the atmosphere and 30×30 km in the tropical ocean),  
87 ensuring a fair comparison. But they have different vertical resolutions in the atmosphere (Table 1),  
88 which are 26 layers with its top at 2.917 hPa in BCC-CSM1.1m and 46 layers with its top at 1.459 hPa  
89 in BCC-CSM2-MR (Figure 1). The present version of BCC-CSM2-MR takes 50% more computing  
90 time than BCC-CSM1.1m for the same amount of parallel computing processors.

## 91 **2.1 Atmospheric component BCC-AGCM**

92 The atmospheric component of BCC-CSM1.1m is BCC-AGCM2.2 (second generation). It is  
93 detailed in a series of publications (Wu et al., 2008, 2010; Wu, 2012; Wu et al., 2013).  
94 BCC-AGCM3-MR is its updated version (third generation), used as the atmosphere component in  
95 BCC-CSM2-MR. The dynamic core in the two models is identical and uses the spectral framework  
96 described in Wu et al. (2008), in which a reference stratified atmospheric temperature and a reference  
97 surface pressure are introduced into the governing equations to improve pressure gradient force and  
98 gradients of surface pressure and temperature, the prognostic variables for temperature and surface  
99 pressure are separately replaced by their perturbations from their references. Explicit time difference  
100 scheme is applied to vorticity equation, and semi-implicit time difference scheme for divergence,  
101 temperature, and surface pressure equations. Semi-Lagrangian tracer transport scheme is used for water  
102 vapor, liquid cloud water and ice cloud water. Main differences of model physics used in the two  
103 models (BCC-AGCM2.2 and BCC-AGCM3-MR) are summarized in Table 2 and details in the  
104 following:

### 105 ***a. Deep convection***

106 Our second-generation atmospheric model, BCC-AGCM2.2, operates with a parameterization  
107 scheme of deep cumulus convection developed by Wu (2012). Main characteristics can be summarized  
108 as follows:

109 (1) Deep convection is initiated at the level of maximum moist static energy above the boundary  
110 layer. It is triggered when there is positive convective available potential energy (CAPE) and if the  
111 relative humidity of the air at the lifting level of convective cloud is greater than 75%;

112 (2) A bulk cloud model taking into account processes of entrainment/detrainment is used to  
113 calculate the convective updraft with consideration of budgets for mass, dry static energy, moisture,  
114 cloud liquid water, and momentum. The scheme also considers the lateral entrainment of the  
115 environmental air into the unstable ascending parcel before it rises to the lifting condensation level. The  
116 entrainment/detrainment amount for the updraft cloud parcel is determined according to the  
117 increase/decrease of updraft parcel mass with altitude. Based on a total energy conservation equation of  
118 the whole adiabatic system involving the updraft cloud parcel and the environment, the mass change for  
119 the adiabatic ascent of the cloud parcel with altitude is derived;

120 (3) The convective downdraft is assumed to be saturated and originated from the level of minimum  
121 environmental saturated equivalent potential temperature within the updraft cloud;

122 (4) The closure scheme determining the mass flux at the base of convective cloud is that suggested  
123 by Zhang (2002). It assumes that the increase/decrease of CAPE due to changes of the thermodynamic  
124 states in the free troposphere resulting from convection approximately balances the decrease/increase  
125 resulting from large-scale processes.

126 A modified version of Wu (2012) is used in BCC-AGCM3-MR for deep convection  
127 parameterization. The convection is triggered only when the boundary layer is unstable or there exists  
128 updraft velocity in the environment at the lifting level of convective cloud, and simultaneously there is  
129 positive CAPE. This modification is aimed to connect the deep convection to the instability of the  
130 boundary layer. The lifting condensation level is set to above the nominal level of non-divergence (600  
131 hPa) in BCC-AGCM2.2 and lowered to the level of 650 hPa in BCC-AGCM3-MR. These modifications  
132 in the deep convection scheme are found to improve the simulation of diurnal cycle of precipitation and  
133 Madden-Julian Oscillation (MJO).

#### 134 ***b. Shallow convection***

135 Shallow convection is parameterized with a local convective transport scheme (Hack, 1994). It is  
136 used to remove any local instability that may remain after the deep convection scheme. This Hack  
137 convection scheme is largely-used one to typically represent shallow subtropical convection and  
138 midlevel convection that do not originate from the boundary layer.

#### 139 ***c. Cloud macrophysics***

140 Cloud macrophysics comprises physical processes to compute cloud fractions in each layer,  
 141 horizontal and vertical overlapping of clouds, and conversion rates of water vapor into cloud  
 142 condensates. In BCC-AGCM2.2, cloud fraction and the associated cloud macrophysics follow what  
 143 designed in NCAR Community Atmosphere Model version 3 (CAM3, Collins et al., 2004). The total  
 144 cloud cover ( $C_{tot}$ ) within each model grid is set as the maximum value of three cloud covers: low-level  
 145 marine stratus ( $C_{mst}$ ), convective cloud ( $C_{conv}$ ), and stratus cloud ( $C_s$ ),

$$146 \quad C_{tot} = \max(C_{conv}, C_{mst}, C_s) \quad (1)$$

147 As in CAM3, the marine stratocumulus cloud is diagnosed with an empirical relationship between the  
 148 cloud fraction and the boundary layer stratification which is evaluated with atmospheric variables at  
 149 surface and 700mb (Klein and Hartmann, 1993). The convective cloud fraction uses a functional form  
 150 of Xu and Krueger (1991) relating the cloud cover to updraft mass flux from the deep and shallow  
 151 convection schemes. The stratus cloud fraction is diagnosed on the basis of relative humidity which  
 152 varies with pressure.

153 A new cloud scheme is developed and used in BCC-AGCM3-MR. It consists of calculating  
 154 convective cloud and the total cloud cover in a different way from BCC-AGCM2.2. The total cloud  
 155 fraction in each model grid cell is given as

$$156 \quad C_{tot} = C_{conv} + (1 - C_{conv}) \max(C_{mst}, C_s) \quad (2)$$

157 And the convective cloud  $C_{conv}$  is assumed to be the sum of shallow ( $C_{shallow}$ ) and deep ( $C_{deep}$ )  
 158 convective cloud fractions:

$$159 \quad C_{conv} = C_{shallow} + C_{deep} \quad (3)$$

160  $C_{shallow}$  and  $C_{deep}$  are non-overlapped with each other and diagnosed following the relationships,

$$161 \quad C_{conv} q^*(T_c) + (1 - C_{conv}) \bar{q} = \bar{q}_{conv} \quad (4)$$

$$162 \quad C_{conv} T_c + (1 - C_{conv}) \bar{T} = \bar{T}_{conv} \quad (5)$$

163 and

$$164 \quad q^*(T_c) = q^*(\bar{T}) + \frac{\partial q^*(\bar{T})}{\partial \bar{T}} (T_c - \bar{T}) \quad (6)$$

165 where  $\bar{q}$  and  $\bar{T}$ ,  $\bar{q}_{conv}$  and  $\bar{T}_{conv}$  denote the model grid box-averaged water vapor mixing ratio and  
 166 temperature in the ‘environment’ before and after convection activity, respectively.  $T_c$  and  $q^*(T_c)$  are  
 167 the temperature inside the convective cloud plume and its saturated water vapor mixing ratio. Here, we  
 168 assume that the shallow and deep convection can concurrently occur in the same atmospheric column at  
 169 any time step. That is, the shallow convection scheme follows the deep convection and occurs at  
 170 vertical layers where local instability still remains after deep convection.

171 If no supersaturation exists in clouds, we can obtain from Eqs. (4) and (5)

$$172 \quad C_{conv} = \frac{(\bar{q}_{conv} - \bar{q}) - \frac{\partial q^*(\bar{T})}{\partial T} (\bar{T}_{conv} - \bar{T})}{q^*(\bar{T}) - \bar{q}}. \quad (7)$$

173 The temperature  $T_c$  and the specific humidity  $q_c = q^*(T_c)$  of the cloud plume can be firstly derived  
 174 from Eqs. (5) and (6). Following the method above, the cloud fraction ( $C_{deep}$  and  $C_{shallow}$ ),  
 175 temperature ( $T_{deep}$  and  $T_{shallow}$ ), specific humidity ( $q_{deep}$  and  $q_{shallow}$ ) for the deep convective,  
 176 shallow convective clouds can be then deduced sequentially.

177 After the three moisture processes (i.e. deep convection, then shallow convection, and finally  
 178 stratiform precipitation) are finished, the mean temperature ( $\bar{T}_{box}$ ) and specific humidity ( $\bar{q}_{box}$ ) of the  
 179 whole model-grid box are then updated. Ambient temperature ( $\bar{T}_{ambient}$ ) and specific humidity  
 180 ( $\bar{q}_{ambient}$ ) outside convective clouds can be finally estimated using the following Eqs.,

$$181 \quad \bar{q}_{box} = \bar{q}_{ambient} \cdot (1 - C_{deep} - C_{shallow}) + q_{deep} \cdot C_{deep} + q_{shallow} \cdot C_{shallow}, \quad (8)$$

182 and

$$183 \quad \bar{T}_{box} = \bar{T}_{ambient} \cdot (1 - C_{deep} - C_{shallow}) + T_{deep} \cdot C_{deep} + T_{shallow} \cdot C_{shallow}. \quad (9)$$

184 Finally, the stratus cloud fraction  $C_s$  is diagnosed on the basis of the relative humidity ( $RH_{ambient}$ ) of  
 185 the ambient,

$$186 \quad C_s = \left( \frac{RH_{ambient} - RH_{min}}{1 - RH_{min}} \right)^2 \quad (10)$$

187 where  $RH_{min}$  is a threshold of relative humidity and  $RH_{ambient}$  is derived with  $\bar{T}_{ambient}$  and  $\bar{q}_{ambient}$ .  
 188 If  $C_{deep} + C_{shallow} > 1$  in Eqs. (8) and (9),  $C_{deep}$  and  $C_{shallow}$  are scaled to meet the condition  
 189  $C_{deep} + C_{shallow} = 1.0$ , and then  $C_s = 0$ . At that condition, we do not calculate  $\bar{T}_{ambient}$  and  
 190  $\bar{q}_{ambient}$  from Eqs. (8) and (9).

#### 191 **d. Cloud microphysics**

192 In BCC-AGCM2.2 and BCC-AGCM3-MR, the essential part of the stratiform cloud microphysics  
 193 remains the same and follows the framework of non-convective cloud processes in CAM 3.0 (Collins et  
 194 al., 2004) that is the scheme proposed by Rasch and Kristjánsson (1998) and modified by Zhang et al.  
 195 (2003). However there is a noticeable difference of cloud microphysics in the two models concerning  
 196 the treatments for indirect effects of aerosols through mechanisms of clouds and precipitation. Indirect  
 197 effects of aerosols were not included in BCC-AGCM2.2 for CMIP5. That is, the cloud droplets  
 198 effective radius was not related to aerosols, neither the precipitation efficiency. The cloud droplets  
 199 effective radius was either prescribed or a simple function of atmospheric temperature. The effective  
 200 radius for warm clouds was specified to be  $14 \mu\text{m}$  over open ocean and sea ice, and was a function of  
 201 atmospheric temperature over land. For ice clouds, the effective radius was also a function of  
 202 temperature following Kristjánsson et al. (2000).

203 Aerosol particles influence clouds and the hydrological cycle by their ability to act as cloud  
 204 condensation nuclei and ice nuclei. This indirect radiative forcing of aerosols is included in the latest  
 205 version of BCC-AGCM3-MR, with the effective radius of liquid water cloud droplets being related to  
 206 the cloud droplet number concentration  $N_{cdnc}$  ( $\text{cm}^{-3}$ ). As proposed by Martin et al. (1994), the  
 207 volume-weighted mean cloud droplet radius  $r_{l,vol}$  can be expressed as

$$208 \quad r_{l,vol} = \left[ (3LWC) / (4\pi\rho_w N_{cdnc}) \right]^{1/3}, \quad (11)$$

209 where  $\rho_w$  is the liquid water density, LWC is the cloud liquid water content ( $\text{g cm}^{-3}$ ). Cloud water  
 210 and ice contents are prognostic variables in our model with source and sink terms taking into account  
 211 the cloud microphysics. The effective radius of cloud droplets  $r_{el}$  is then estimated as

$$212 \quad r_{el} = \beta \cdot r_{l,vol} \quad (12)$$

213 where  $\beta$  is a parameter dependent on the droplets spectral shape. There are various methods to  
 214 parameterize it (e.g. Pontikis and Hicks, 1992; Liu and Daum, 2002). We use the calculation proposed  
 215 by Peng and Lohmann (2003),

$$216 \quad \beta = 0.00084 N_{cdnc} + 1.22 \quad (13)$$

217 In BCC-AGCM3-MR, the liquid cloud droplet number concentration  $N_{cdnc}$  ( $\text{cm}^{-3}$ ) is a diagnostic  
 218 variable dependent on aerosols mass. It is explicitly calculated with the empirical function suggested by  
 219 Boucher and Lohmann (1995) and Quaas et al. (2006) :

$$220 \quad N_{cdnc} = \exp[5.1 + 0.41 \ln(m_{aero})] \quad (14)$$

221 The total aerosols mass is the sum of four types of aerosol,

$$222 \quad m_{aero} = m_{SS} + m_{OC} + m_{SO_4} + m_{NH_4NO_3} \cdot \quad (15)$$

223 Here,  $m_{aero}$  ( $\mu\text{g}\cdot\text{m}^{-3}$ ) is the total mass of all hydrophilic aerosols, i.e., the first bin (0.2 to 0.5  $\mu\text{m}$ ) of  
 224 sea salt ( $m_{SS}$ ), hydrophilic organic carbon ( $m_{OC}$ ), sulphate ( $m_{SO_4}$ ), and nitrate ( $m_{NH_4NO_3}$ ). Nitrate as a  
 225 rapidly increasing aerosol species in recent years affects present climate and potentially has large  
 226 implications on climate change (Xu and Penner, 2012; Li et al., 2014). A dataset of nitrate from NCAR  
 227 CAM-Chem (Lamarque et al., 2012) is used in our model.

228 Aerosols also exert impacts on precipitation efficiency (Albrecht, 1989), which is taken into  
 229 account in the parameterization of non-convective cloud processes. We use the same scheme as in  
 230 CAM3 (Rasch and Kristjánsson, 1998; Zhang et al., 2003). There are five processes that convert  
 231 condensate to precipitate: auto-conversion of liquid water to rain, collection of cloud water by rain,  
 232 auto-conversion of ice to snow, collection of ice by snow, and collection of liquid by snow. The  
 233 auto-conversion of cloud liquid water to rain (PWAUT) is dependent on the cloud droplet number  
 234 concentration and follows a formula that was originally suggested by Chen and Cotton [1987],

$$235 \quad PWAUT = C_{l,aut} \frac{q_l^2 \rho_a}{\rho_w N_{ncdc}} \left( \frac{q_l \rho_a}{\rho_w N_{ncdc}} \right)^{1/3} H(r_{l,vol} - r_{ic,vol}) \quad (16)$$

236 Where  $\hat{q}_l$  is in-cloud liquid water mixing ratio,  $\rho_a$  and  $\rho_w$  are the local densities of air and water  
 237 respectively, and

$$C_{l,drag} = 0.55\pi^{1/3}k(3/4)^{4/3}(1.1)^4. \quad (17)$$

In which  $k = 1.18 \times 10^6 \text{ cm}^{-1} \text{ sec}^{-1}$  is the Stokes constant.  $H(x)$  is the Heaviside step function with the definition,

$$H(x) = \begin{cases} 0, & x < 0 \\ 1, & x \geq 0 \end{cases} \quad (18)$$

$r_{lc,vol}$  is the critical value of mean volume radius of the liquid cloud droplets  $r_{l,vol}$ , and set to  $15 \mu \text{ m}$ .

#### *e. Gravity wave drag*

Gravity waves can be generated by a variety of sources including orography, convection, and geostrophic adjustment in regions of baroclinic instability (Richter et al., 2010). Gravity waves propagate upward from their source regions and break when large amplitudes are attained. This produces a drag on the mean flow. Gravity wave drag plays an important role in explaining the zonal mean flow and thermal structure in the upper atmosphere.

In previous versions of BCC models, the orographic gravity wave drag was parameterized as in McFarlane (1987), but non-orographic sources [such as convection and jet-front systems](#) were not considered. In BCC-AGCM3-MR, the gravity wave drag generated from convective sources is introduced as in Beres et al. (2004), but drag by [frontal gravity waves and orographic](#) blocking effects [are](#) still not involved. The key point of the Beres' scheme is relating the momentum flux phase speed spectrum to the convective heating properties. In the present version of BCC-AGCM3-MR, the convective gravity wave parameterization is activated only when the deep convective heating depth is greater than 2.5 km. [Gravity waves generated by topography and fronts are important for the higher latitudes. The efficiency parameter in the McFarlane scheme is set to 0.125 in BCC-AGCM2.2 and doubled to 0.25 in BCC-AGCM3-MR to obtain a better result of the polar night jet. In future, more work will be done it is planned to improve the orographic gravity wave scheme, and to implement parameterizations of gravity waves emitted by fronts and jets.](#)

[In the convective gravity wave scheme,](#) the uncertainty in the magnitude of momentum flux arises from the horizontal scale of the heating and the convective fraction. The convective fraction (CF) within a grid cell is an important parameter and can be tuned to obtain right wave amplitudes. It is a

264 constant and valid for all latitudes where convection is active. Previous studies of Alexander et al. (2004)  
 265 show that CF can vary from ~0.2% to ~7%–8%. We use 5% in BCC-AGCM3-MR. This  
 266 parameterization scheme of convective gravity waves can improve the model’s ability to simulate the  
 267 stratospheric quasi-biennial oscillation in BCC-AGCM3-MR.

268 ***f. Radiative transfer***

269 The radiative transfer parameterization in BCC-AGCM2.2 follows the scheme initially  
 270 implemented in CAM3 (Collins et al., 2004). Aerosol indirect effects on radiation are not taken into  
 271 account and cloud droplets effective radius is only function of temperature for cold clouds and  
 272 prescribed to different values for maritime, polar, and continental cases for warm clouds. In  
 273 BCC-AGCM3-MR, however, the aerosol indirect effects are fully included and the effective radius of  
 274 droplets for liquid clouds is calculated by Equation (12) using the liquid cloud droplet number  
 275 concentration.

276 ***g. Boundary layer turbulence***

277 BCC-AGCM3-MR basically inherits the boundary layer turbulence parameterization used in  
 278 BCC-AGCM2.2, which is based on the eddy diffusivity approach (Holtslag and Boville, 1993). The  
 279 eddy diffusivity is given by

$$280 \quad K_c = kw_t z \left(1 - \frac{z}{h}\right)^2, \quad (19)$$

281 where  $w_t$  is a turbulent velocity and  $h$  is the boundary layer height, which is estimated as

$$282 \quad h = z_s + \frac{Ri_c \left\{ [u(h) - u_{SL}]^2 + [v(h) - v_{SL}]^2 + \beta u_*^2 \right\}}{(g/\theta_{SL}) [\theta_v(h) - \theta_{SL}]}, \quad (20)$$

283 where  $z_s$  is the height of the lowest model level,  $u$ ,  $v$ , and  $\theta_v$  are horizontal wind components and  
 284 virtual potential temperature at height  $z$ ,  $u_{SL}$ ,  $v_{SL}$ , and  $\theta_{SL}$  represent the same variables, but in the  
 285 surface layer.  $\beta$  in Eq. (20) is a constant and taken as 100.  $u_*$  is the friction velocity, and  $g$  is  
 286 gravitational acceleration.

287 The critical Richardson number  $Ri_c$  in Eq. (20) is a key parameter for calculating the boundary layer  
 288 height and is set to a constant (0.3) for all stable conditions in BCC-AGCM2.2. In BCC-AGCM3-MR,

289  $R_i$  varies according to conditions of boundary layer stability to yield more accurate estimates of  
290 boundary layer height, and set to 0.24 for strongly stable conditions, 0.31 for weakly stable conditions,  
291 and 0.39 for unstable conditions based on observational studies of Zhang et al. (2014).

## 292 **2.2 Land component BCC-AVIM**

293 BCC-AVIM, Beijing Climate Center Atmosphere-Vegetation Interaction Model, is a  
294 comprehensive land surface scheme developed and maintained in BCC. The version 1 (BCC-AVIM1.0)  
295 was used as the land component in BCC-CSM1.1m participating in CMIP5 (Wu et al., 2013). It  
296 includes major land surface biophysical and plant physiological processes. Its origin could go back to  
297 the Atmosphere-Vegetation Interaction Model (AVIM) (Ji, 1995; Ji et al., 2008) with the necessary  
298 framework to include biophysical, physiological, and soil carbon-nitrogen dynamical processes. The  
299 biophysical module in BCC-AVIM1.0, with 10 layers for soil and up to five layers for snow, is almost  
300 the same as that used in the NCAR Community Land Model version 3 (CLM3) (Oleson et al., 2004).  
301 The terrestrial carbon cycle in BCC-AVIM1.0 consists of a series of biochemical and physiological  
302 processes modulating photosynthesis and respiration of vegetation. Carbon assimilated by vegetation is  
303 parameterized by a seasonally varying allocation of carbohydrate to leaves, stem, and root tissues as a  
304 function of the prognostic leaf area index. Litter due to turnover and mortality of vegetation, and carbon  
305 dioxide release into atmosphere through the heterogeneous respiration of soil microbes is taken into  
306 account in BCC-AVIM1.0. Vegetation litter falls to the ground surface and into the soil is divided into  
307 eight idealized terrestrial carbon pools according to the timescale of carbon decomposition of each pool  
308 and transfers among different pools, which is similar to that in the carbon exchange between vegetation,  
309 soil and the atmosphere (CEVSA) model (Cao and Woodward, 1998).

310 BCC-AVIM1.0 has been updated to BCC-AVIM2.0 which serves as the land component of  
311 BCC-CSM2-MR participating in CMIP6. As listed in Table 3, several improvements have been  
312 implemented in BCC-AVIM2.0, such as the inclusion of a variable temperature threshold to determine  
313 soil water freezing/thawing rather than fixed at 0°C, a better calculation of snow surface albedo and  
314 snow cover fraction, a dynamic phenology for deciduous plant function types, and a four-stream  
315 approximation on solar radiation transfer through vegetation canopy. Besides, a simple scheme for  
316 surface fluxes over rice paddy is also implemented in BCC-AVIM2.0. These improvements are briefly

317 discussed as follows.

318 (a) Soil water freezes at the constant temperature 0 °C in BCC-AVIM1.0, but the actual  
319 freezing-thawing process is a slowly and continuously changing process. We take into account the fact  
320 that the soil water potential remains in equilibrium with the water vapor pressure over pure ice when  
321 soil ice is present. Based on the relationships among soil water matrix potential  $\psi$  (mm), soil  
322 temperature and soil water content, a variable temperature threshold for freeze-thaw dependent on soil  
323 liquid water content, soil porosity and saturated soil matrix potential is introduced. The inclusion of this  
324 scheme improves the performance of BCC-AVIM2.0 in the simulation about seasonal frozen soil (Xia et  
325 al., 2011).

326 (b) In BCC-AVIM1.0, we took into account the snow aging effect on surface albedo with a simple  
327 consideration by using a unified scheme to mimic the snow surface albedo decrease with time. In  
328 BCC-AVIM2.0, we assume different reduction rates of snow albedo with actual elapsed time after  
329 snowfalls in the accumulating and melting stages of a snow season (Chen et al., 2014). Besides, the  
330 variability of sub-grid topography is now taken into account to calculate the snow cover fraction within  
331 a model grid cell.

332 (c) Unlike the empirical plant leaf unfolding and withering dates prescribed in BCC-AVIM1.0, a  
333 dynamic determination of leaf unfolding, growth, and withering dates according to the budget of  
334 photosynthetic assimilation of carbon similar to the phenology scheme in CTEM (Arora, 2005) was  
335 implemented in BCC-AVIM2.0. Leaf loss due to drought and cold stresses in addition to natural  
336 turnover are also considered.

337 (d) The four-stream solar radiation transfer scheme within canopy in BCC-AVIM2.0 is based on  
338 the same radiative transfer theory used in atmosphere (Liou, 2004). It adopts the analytic formula of  
339 Henyey-Greenstein for the phase function. The vertical distribution of diffuse light within canopy is  
340 related to transmissivity and reflectivity of leaves, besides, average leaf angle and direction of incident  
341 direct beam radiation influence diffuse light within canopy as well. The upward and downward radiative  
342 fluxes are determined by the phase function of diffuse light, G-function, leaf reflectivity and  
343 transmissivity, leaf area index, and the cosine of solar angle of incident direct beam radiation (Zhou et al.,  
344 2018).

345 (e) Considering the wide distribution of rice paddies in Southeast Asia and the quite different  
346 characteristics of rice paddies and bare soil, a scheme to parameterize the surface albedo, roughness  
347 length, turbulent sensible and latent heat fluxes over rice paddies is developed (a manuscript is in  
348 preparation) and implemented in BCC-AVIM2.0.

349 (f) Finally, land-use and land-cover changes are explicitly involved in BCC-AVIM2.0. An increase  
350 in crop area implies the replacement of natural vegetation by crops, which is often known as  
351 deforestation.

### 352 **2.3 Ocean and Sea Ice**

353 There are no significant changes for the ocean and sea ice from BCC-CSM1.1m to  
354 BCC-CSM2-MR. But for the sake of completeness, we present here a short description of them. The  
355 oceanic component is MOM4-L40, an oceanic GCM. It was based on the Z-coordinate Modular Ocean  
356 Model (MOM), version 4 (Griffies, 2005) developed by the Geophysical Fluid Dynamics Laboratory  
357 (GFDL). It has a nominal resolution of  $1^\circ \times 1^\circ$  with a tri-pole grid, the actual resolution being from  $1/3^\circ$   
358 latitude between  $30^\circ \text{S}$  and  $30^\circ \text{N}$  to  $1.0^\circ$  at  $60^\circ$  latitude. There are 40 z-levels in the vertical. The two  
359 northern poles of the curvilinear grid are distributed to land areas over Northern America and over the  
360 Eurasian continent. There are 13 vertical levels placed between the surface and the 300-m depth of the  
361 upper ocean. MOM4\_L40 adopts some mature parameterization schemes, including Swedy's  
362 tracer-based third order advection scheme, isopycnal tracer mixing and diffusion scheme (Gent and  
363 McWilliams, 1990), Laplace horizontal friction scheme, KPP vertical mixing scheme (Large et al.,  
364 1994), complete convection scheme (Rahmstorf, 1993), overflow scheme of topographic processing of  
365 sea bottom boundary/steep slopes (Campin & Goosse, 1999), and shortwave penetration schemes based  
366 on spatial distribution of chlorophyll concentration (Sweeney et al., 2005).

367 Concentration and thickness of sea ice are calculated by the Sea Ice Simulator (SIS) developed by  
368 GFDL (Winton, 2000). It is a global sea ice thermodynamic model including the Elastic-Viscous-  
369 Plastic dynamic process and Semtner's thermodynamic process. SIS has 3 vertical layers, including 1  
370 snow cover and 2 ice layers of equal thickness. In each grid, 5 categories of sea ice (including open  
371 water) are considered, according to the thickness of sea ice. It also takes into account the mutual  
372 transformation from one category to another under thermodynamic conditions. The sea ice model

operates on the same oceanic grid and has the same horizontal resolution of MOM\_L40. SIS calculates concentration, thickness, temperature, salinity of sea ice and motions of snow cover and ice sheet. There is no gas exchange through sea ice.

#### 2.4. Surface turbulent fluxes between air and sea/sea ice

The atmosphere and sea/sea ice interplay through the exchange of surface turbulent fluxes of momentum, heat and water. An optimum treatment of the surface exchange, sound in physics and economic in computation, is very important in simulating the climate variability. During the past years, we maintain a continuous effort to improve the turbulent exchange processes between air and sea/sea ice in different versions of BCC models.

In BCC-CSM1.1m, the bulk formulas of turbulent fluxes over sea surface originate from those used in CAM3, with some modifications to the roughness lengths and corrections to the temperature and moisture gradients considering sea spray effects (Wu et al., 2010). The bulk formulas are updated in BCC-CSM2-MR. The coefficients in roughness lengths calculations were adjusted and the arbitrary gradient corrections are not used. Instead, a gustiness parameterization is included to account for the subgrid wind variability that is contributed by boundary layer eddies, convective precipitation, and cloudiness (Zeng et al., 2002).

In terms of turbulent exchange between air and sea ice, we proposed a new bulk algorithm aiming to improve flux parameterizations over sea ice (Lu et al., 2013). Based on theoretical and observational analysis, the new algorithm employs superior stability functions for stable stratification as suggested by Zeng et al. (1998), and features varying roughness lengths. All the three roughness lengths ( $z_0$ ,  $z_T$ ,  $z_Q$ ) of sea ice were set to a constant (0.5 mm) in BCC-CSM1.1m. Observational studies show that values of  $z_0$  tend to be smaller than 0.5 mm over sea ice in winter and larger than 0.5 mm in summer (Andreas et al., 2010a; Andreas et al., 2010b). In the new parameterization used in BCC-CSM2-MR, the roughness lengths for momentum differentiate between warm and cold seasons. For simplicity,  $z_0$  is treated as

$$z_0(mm) = \begin{cases} 0.1 & \text{for } T_s \leq -2^\circ C \\ 0.8 & \text{for } T_s > -2^\circ C \end{cases}, \quad (19)$$

where  $T_s$  represents surface temperature. For the scalar roughness lengths, a theoretical-based model proposed by Andreas (1987) is used in the new scheme. This model expresses the scalar roughness  $z_s$

400 ( $z_T$  or  $z_Q$ ) as a function of the roughness Reynolds number  $R^*$ , i.e.,

$$401 \quad \ln(z_s/z_0) = b_0 + b_1(\ln R_s) + b_2(\ln R_s)^2. \quad (20)$$

402 Andreas (1987, 2002) tabulates the polynomial coefficients  $b_0$ ,  $b_1$  and  $b_2$ .

### 403 3. Experimental design

404 All BCC simulations presented in this work follow the protocols defined by CMIP5 and CMIP6.  
405 We pay attention for them to be comparable in spite of showing the transition of our climate system  
406 model from CMIP5 to CMIP6. The principal simulation to be analyzed is the historical simulation  
407 (hereafter historical) with prescribed forcings from 1850 to 2005 for CMIP5 (to 2014 for CMIP6).

408 Historical forcings data are based as far as possible on observations and downloaded from the  
409 webpage (<https://esgf-node.llnl.gov/search/input4mips/>). They mainly include: (1) GHG concentrations  
410 (only CO<sub>2</sub>, N<sub>2</sub>O, CH<sub>4</sub>, CFC11, CFC12 used in BCC models) with zonal-mean values and updated  
411 monthly; (2) Yearly global gridded land-use forcing; (3) Solar forcing; (4) Stratospheric aerosols (from  
412 volcanoes); (5) CMIP6-recommended anthropogenic aerosol optical properties which is formulated in  
413 terms of nine spatial plumes associated with different major anthropogenic source regions (Stevens et  
414 al., 2017). (6) Time-varying gridded ozone concentrations. In addition, aerosol masses based on CMIP5  
415 (Taylor et al., 2012) are used for on-line calculation of cloud droplet effective radius in BCC model.

416 The preindustrial initial state of BCC-CSM2-MR is preceded by a 500-years piControl simulation  
417 following the requirement of CMIP6. The initial state of the piControl simulation itself is obtained  
418 through individual spin-up runs of each component of BCC-CSM2-MR in order for piControl  
419 simulation to run stably and fast to its model equilibrium. Actually, the initial states of atmosphere and  
420 land are obtained from a 10-years AMIP run forced with monthly climatology of sea surface  
421 temperature (SST) and sea ice concentration, and the initial states of ocean and sea ice are derived from  
422 a 1000-years forced run with a repeating annual cycle of monthly climatology of atmospheric state from  
423 the Coordinated Ocean-Ice Reference Experiment (CORE) dataset version 2 (Danabasoglu et al., 2014).  
424 Figure 2 shows time series of the annual and global mean of net energy flux at top of the atmosphere  
425 (TOA) and the sea surface temperature for 600 years in the piControl simulation. The whole system in  
426 BCC-CSM2-MR ~~nearly fluctuates around +0.4 W m<sup>-2</sup> net energy flux at TOA without obvious trend~~  
427 ~~reaches its equilibrium after in~~ 600 years. ~~The global mean surface air temperature~~ ~~has~~ ~~shows~~ ~~a~~ ~~little~~

~~bits~~small warming after 600 years (Fig. 2b). During the last~~te~~ 300 years, there ~~is near~~ are ( $\pm 0.2$  K amplitude) oscillations of centennial scale ~~averaged~~ for the whole globe and a little weak for the area average of 60°S to 60°N ~~in centennial scale. It is, to a large extent,~~ They are certainly caused by internal variation ~~in~~ of the whole system.

#### 4. Evaluation and comparison between BCC CMIP5 and CMIP6 models

##### 4.1 Global Energy Budget

Radiative fluxes at the top of the model atmosphere are fundamental variables characterizing the Earth's energy balance. Satellite observations in modern time allow us to monitor changes in the net radiation at top-of-atmosphere (TOA) from 2001 onwards. CERES (Clouds and Earth's Radiant Energy System) project, with the lessons learned from its predecessor, the Earth's Radiation Budget Experiment (ERBE), provides improved observation-based data products of Earth's radiation budget (Wielicki et al., 1996). Recently, data of CERES are synthesized with EBAF (Energy Balanced and Filled) data to derive the CERES-EBAF products, suitable for evaluation of climate models (Loeb et al., 2012). As shown in Table 4, the TOA shortwave and longwave components in BCC-CSM2-MR are generally closer to CERES-EBAF compared to those in BCC-CSM1.1m. Model results are for the period 1986–2005, while the available CERES-EBAF data are for 2003–2014. Globally-averaged TOA net energy is  $0.85 \text{ W m}^{-2}$  in BCC-CSM2-MR and  $0.98 \text{ W m}^{-2}$  in BCC-CSM1.1m for the period from 1986 to 2005. The energy equilibrium of whole earth system in BCC-CSM2-MR is slightly improved.

Clouds constitute a major modulator of the radiative transfer in the atmosphere for both solar and terrestrial radiations. Their macro and micro properties, including their radiative properties exert strong impacts on the equilibrium and variation of the radiative budget at TOA or at surface. Figure 3 displays annual and zonal mean of shortwave, longwave and net cloud radiative forcing for BCC CMIP5 (blue curves), CMIP6 (red curves) models and observations (black curves). The data used in Fig. 3 are the same as in Table 4. Although observations and models results cover different time periods, they are still relevant to reveal climatological mean performance of climate models. In low latitudes between 30°S and 30°N, BCC-CSM1.1m shows excessive cloud radiative forcing for both shortwave and longwave radiations. These biases are largely reduced in BCC-CSM2-MR, which is possibly attributed to the new algorithm of cloud fraction especially for convective cloud amount. Cloud radiative forcing in mid

456 latitudes shows large uncertainty, also manifested in the large deviation between the two observations.  
457 Cloud radiative forcing in both models is closer to CERES-EBAF than to CERES in mid latitudes. It is  
458 clear that the new physics modifies the simulated climate and cloud properties, including the fractional  
459 coverage of clouds, their vertical distribution as well as their liquid water and ice content.

#### 460 **4.2. Performance in Simulating the Global Warming in the 20<sup>th</sup> Century**

461 The historical simulation allows us to evaluate the ability of models to reproduce the global  
462 warming and climate variability in the 20th century. The performance depends on both model  
463 formulation and the time-varying external forcings imposed on the models (Allen et al., 2000). Figure 4  
464 presents global-mean (from 60° S to 60° N) surface air temperature evolutions from HadCRUT4 (Morice  
465 et al., 2012) and BCC CMIP5 and CMIP6 models. Here only the area from 60° S to 60° N is used for  
466 comparison, since few observations existed in polar regions to deduce reliable information in  
467 HadCRUT4, especially before the 20th century. To better reveal long-term trends, the climatological  
468 mean is calculated for the reference period 1961–1990 and removed from the time series. The  
469 interannual variability of both simulations is qualitatively comparable to that observed. When a  
470 [119-year](#) smoothing is applied, the long-term trend of both CMIP6 and CMIP5 models is highly  
471 correlated with HadCRUT4. Figure 4 presents three members of historical simulations from different  
472 initial state of the piControl simulation. The correlation coefficients are 0.90 in CMIP5 and 0.93, 0.93,  
473 0.90 in three members of CMIP6, respectively.

474 A remarkable feature in Figure 4 is the presence of a global warming hiatus or pause for the period  
475 from 1998 to 2013 when the observed global surface air temperature warming slowed down. This is a  
476 hot topic, largely debated in the scientific research community (e.g. Fyfe et al., 2016; Medhaug et al.,  
477 ~~2017). There are two members (r1i1p1f1 and r2i1p1f1 in Fig. 4) of historical simulations of the CMIP6~~  
478 ~~model show a hiatus towards the end of the simulation that resembles the observed one. , -and +~~[Although](#)  
479 [the third member \(r3i1p1f1\) simulated the trend of a global warming slowdown during the period from](#)  
480 [2004 to 2012, it is not comparable to the observed hiatus as it has a short spell of colder years centered](#)  
481 [at 2010. shows a decreased trend of warming in the same period. Another warming hiatus occurred in  
482 the period of 1942 to 1974. The first and the third members \(r1i1p1f1 and r3i1p1f1\) of BCC-CSM2-MR  
483 only simulate the warming slowdown in the late period from 1958 to 1974, but the second member](#)

484 (r2i1p1f1) of BCC-CSM2-MR almost simulate this warming hiatus in the whole period from 1942 to  
485 1974. ~~The reason why the BCC CMIP6 model simulates both periods of global warming hiatus is~~  
486 ~~beyond the scope of this paper and will be explored in future. So, the simulation of global warming~~  
487 ~~hiatus in BCC CMIP6 model clearly excludes any simple response to forcing, and makes internal~~  
488 ~~variability a much more likely reason.~~

489 The models response of the SAT to volcanic forcing is slightly stronger than that estimated with  
490 HadCRU data. Evident global cooling shocks are coincident with significant volcanic eruptions such as  
491 Krakatoa (in 1883), West Indies Agung (in 1963), and Mount Pinatubo (in 1991). Each of these  
492 volcanic eruptions significantly enriched stratospheric aerosols (available from  
493 <http://data.giss.nasa.gov/modelforce/strataer/>). As shown in Figure 4, SAT may decrease by up to 0.4 °C  
494 within 1 to 2 years after major volcanic eruptions. The substantial cooling response to volcanic  
495 eruptions is, to a great extent, due to the aerosol direct radiative forcing too strong in both versions of  
496 BCC-CSM.

497 To keep the paper concise and at a reasonable length, only the first member of CMIP6 historical  
498 simulations of BCC-CSM2-MR will be presented hereafter. Biases of annual mean surface air  
499 temperature (at 2 meters) in the whole globe for BCC-CSM2-MR and BCC-CSM1.1m are shown in  
500 Figure 5. In both BCC models, biases are generally within  $\pm 3$  °C, but there are slightly systematic  
501 warm biases over oceans from 50 °S to 50 °N and systematic cold ones over most land regions in north  
502 of 50 °N, in East Asia and in North Africa. Cold biases in high latitudes of the Northern Hemisphere  
503 (North Atlantic, Arctic, North America and Siberia) seem amplified in BCC-CSM2-MR. The land  
504 surface biases in both coupled models are similar to each other. Those patterns of biases are already  
505 present in AMIP simulations (not shown), where effects of oceanic biases are excluded. So those biases  
506 in land surface partly come from their land surface modelling component. In the Southern Ocean, both  
507 models show a strong warm area in the Weddell Sea. BCC-CSM1.1m shows cold biases in other  
508 regions of the Southern Ocean. The disappearance of cold biases in the Southern Oceans in  
509 BCC-CSM2-MR is possibly attributed to the new scheme of cloud fraction (Table 2) as there is a zone  
510 of low-level cloud between 40 °S to 60 °S in the Southern Ocean (omitted), not only in models but also  
511 in observations.

512 **4.3 Climate sensitivity to CO<sub>2</sub> increasing**

513 The long trend of global warming in Figure 4 depends on the climate sensitivity which is an  
514 emblematic parameter to characterize the sensitivity of a climate model to external forcing, with all  
515 feedbacks included. It generally designates the variation of global mean surface air temperature in  
516 response to a forcing of doubled CO<sub>2</sub> concentration in the atmosphere (IPCC 2013). As commonly  
517 practiced in the climate modelling community, an equilibrium climate sensitivity and a transient climate  
518 response can be separately evaluated, corresponding to a situation of equilibrium and transient states of  
519 climate.

520 We use the standard simulation of 1% CO<sub>2</sub> increase per year (1pctCO<sub>2</sub>) to calculate the transient  
521 climate response (TCR), while the equilibrium climate sensitivity (ECS) uses the 4xCO<sub>2</sub> abrupt-change  
522 simulation by applying the forcing/response regression methodology proposed by Gregory et al. (2004).  
523 The TCR is calculated using the difference of annual surface air temperature between the pre-industrial  
524 experiment and a 20-year period centered on the time of CO<sub>2</sub> doubling in 1pctCO<sub>2</sub>, which is 1.71 for  
525 BCC-CSM2-MR and 2.02 for BCC-CSM1.1m. The ECS is diagnosed from the 150-year run of abrupt  
526 4xCO<sub>2</sub> following the approach of Gregory (2012). The method is based on the linear relationship  
527 (Figure 6) governing the changes of net top-of-atmosphere downward radiative flux and the surface air  
528 temperature simulated in abrupt 4xCO<sub>2</sub> relative to the pre-industrial experiment. The ECS is equal to a  
529 half of the temperature change when the net downward radiative flux reaches zero (Andrews et al.,  
530 2012). It is assumed here that 2xCO<sub>2</sub> forcing is half of that for 4xCO<sub>2</sub>, hypothesis generally verified in  
531 climate models. As shown in Fig. 6, the ECS is 3.03 for BCC-CSM2-MR and 2.89 for BCC-CSM1.1m.  
532 So the TCR of the new version model BCC-CSM2-MR is lower than BCC-CSM1.1m, but the ECS of  
533 BCC-CSM2-MR is slightly higher than BCC-CSM1.1m.

534 The linear regression line shown in Figure 6, as pointed out in Gregory et al. (2012), also allows  
535 estimating the instantaneous forcing due to CO<sub>2</sub> increase, and eventually feedbacks parameter of the  
536 climate system. The former is the cross point of the linear regression line with Y axis: 6.2 W m<sup>-2</sup> for  
537 BCC-CSM2-MR and 7.6 W m<sup>-2</sup> for BCC-CSM1.1m. They can be scaled to the case of 2xCO<sub>2</sub> just with  
538 a division factor of 2. Since ECS values are close to each other in the two models, we can easily deduce  
539 that all-feedback factor is larger in BCC-CSM2-MR than in BCC-CSM1.1m. It is actually not

540 surprising to see differences of  $2\times\text{CO}_2$  radiative forcing between the two models even the radiative  
541 transfer scheme is kept identical, because changes in 3-D structures of cloud, atmospheric temperature  
542 and water vapor do exert impacts on additional radiative forcing due to  $\text{CO}_2$  increase in the atmosphere.  
543 It is however interesting to note that feedbacks can operate, in the two models, in such a different way  
544 that ECS keeps almost unchanged between them. ~~This is possibly attributed to the same radiative~~  
545 ~~transfer scheme used in BCC-CSM2-MR and BCC-CSM1.1m (Table 2). We remind that this is a pure~~  
546 ~~coincidence since we did not intentionally tune our model for its sensitivity.~~

#### 547 **4.4 Behaviors of the atmosphere at present day**

548 The main spatial patterns of observed precipitation climatology are simulated in BCC-CSM1.1m  
549 and BCC-CSM2-MR. Figure 7 shows model biases of annual-mean precipitation for BCC-CSM1.1m  
550 and BCC-CSM2-MR in the globe. They are very close from each other. Their RMSE is also very close:  
551 1.12 mm/day against 1.18 mm/day. Regions of lack of precipitation, such as North India, South China,  
552 the two sides of Sumatra, and the Amazon, experience significant amelioration in the new model.  
553 Excessive rainfalls in Tropical Africa, in the Indian Ocean, in the Maritime Continent seem amplified in  
554 BCC-CSM2-MR. As for the whole globe, the annual mean precipitation coming from convective  
555 process (including deep and shallow convections) accounts for 50% of the total precipitation (2.94  
556 mm/day) in BCC-CSM2-MR and 48% of the total precipitation (2.87 mm/day) in BCC-CSM1.1m. The  
557 convective precipitation increased in BCC-CSM2-MR, and the total amount of precipitation exceeds the  
558 amount (2.68 mm/day) of 1986-2005 mean observed precipitation analyses from Global Precipitation  
559 Climatology Project (Adler et al., 2003). But in some regions such as in the Maritime Continent, stratus  
560 precipitation evidently enhances in BCC-CSM2-MR, where the ratio of convection precipitation to total  
561 precipitation is 39% and even larger than 35% in BCC-CSM1.1m.

562 We now use the Taylor diagram (Figure 8) to evaluate the general performance of our two models  
563 in terms of temperature at 850hPa, precipitation and atmospheric general circulation. The evaluation is  
564 done against climatology of ERA-Interim dataset for the period of 1986 to 2005 (Dee et al., 2011).  
565 ERA-Interim is the latest global atmospheric reanalysis produced by the European Centre for  
566 Medium - Range Weather Forecasts (ECMWF).

567 For global fields, we calculate the spatial pattern correlations between models and ERA-Interim

568 ~~dataset~~ for the annual-mean climatology of sea level pressure (SLP), temperature at 850 hPa level  
569 (T850), zonal and meridional wind velocity at 850 hPa (U850 and V850), ~~and zonal wind velocity~~ at  
570 200 hPa (U200), ~~and~~ geopotential height at 500hPa (Z500), and precipitation from Global Precipitation  
571 Climatology Project ~~dataset of precipitation~~ (PRCP in Fig. 8, Adler and Chang, 2003) over the period  
572 1980–2000. Except for PRCP~~precipitation~~ and U850~~zonal wind at 850 hPa~~ which have lower  
573 correlation (less than 0.90) with observation, ~~correlations for~~ other variables are all above 0.90 ~~for their~~  
574 correlation coefficients. The pattern correlation coefficient of Z500~~geopotential height at 500hPa~~ with  
575 ERA-Interim is 0.995, the best correlation among these variables. Except for V850, correlations of all  
576 other variables in CMIP6 model version (BCC-CSM2-MR) have an evident improvement compared to  
577 CMIP5 version (BCC-CSM1.1m). The normalized standard deviations of most variables except for  
578 PRCP~~the precipitation~~ and T850 are obviously improved in BCC-CSM2-MR. As a whole, the  
579 performances of most variables in BCC-CSM2-MR are better than those in BCC-CSM1.1m.

580 Results shown in the Taylor diagrams in Figure 8 about improvements in surface climate and  
581 atmospheric general circulation at different vertical levels are consistent with improvements in the  
582 vertical distribution of atmospheric temperature. Figure 9 shows the yearly-averaged zonal mean of  
583 atmospheric temperature biases in BCC-CSM2-MR and BCC-CSM1.1m, with ERA-Interim for the  
584 period of 1986–2005 as reference. Overall, both BCC-CSM2-MR and BCC-CSM1.1m have similar  
585 biases in their vertical structure, with 1–3 K warmer in the stratosphere (above 100 hPa) for most of the  
586 domain equatorward of 70°N and 70°S. There are larger cold biases near the tropopause (centered near  
587 200hPa) for southward of 30°S and northward of 30°N. In the middle to lower troposphere (below  
588 400hPa), there is a warm bias of 1-2K. Improvements in BCC-CSM2-MR are mainly located in the  
589 troposphere below 100 hPa. Both cold biases near the tropopause in high latitudes and warm bias in  
590 lower latitudes are reduced.

591 The improvement in tropospheric temperature induces naturally smaller biases for the zonal wind  
592 in the whole troposphere in BCC-CSM2-MR (Figure 9). But there are still westerly wind biases of 6  
593  $\text{m s}^{-1}$  in the layer of 100-200 hPa in the tropics. Westerly jets at mid-latitudes are slightly too strong in  
594 both hemispheres. The zonal mean of zonal wind biases in the high latitudes of the stratosphere in  
595 BCC-CSM2-MR have increased near 10 hPa. ~~where t~~ The too-strong polar night jets clearly indicate

596 ~~an insufficient atmospheric too weak drag at this level. It may be~~ ~~where model biases may be~~ partly  
597 caused by ~~not yet involved~~ the lack of effects in relation to some non-orographic gravity waves gravity  
598 ~~wave drag that~~ generated by ~~the sources such as atmospheric fronts and jets blocking effects~~. We expect  
599 to reduce this model bias in next version by adding this process.

600 Given a much higher vertical resolution and an advanced parameterization of the gravity wave  
601 drag, the new model BCC-CSM2-MR is able to represent the stratospheric quasi-biennial oscillation  
602 (QBO), as shown in Figure 10 which displays time-height diagrams of the tropical zonal winds  
603 averaged from 5°S to 5°N. The three panels show observations from the ERA-Interim reanalysis and  
604 relevant simulation results from the two models in CMIP6 and CMIP5. Figure 10a shows alternative  
605 westerlies and easterlies in the lower stratosphere appearing with a mean period of about 28 months in  
606 the ERA-Interim reanalysis. In Figure 10b, the BCC-CSM2-MR simulations present a clear  
607 quasi-biennial oscillation of the zonal winds as observed. In this study, the QBO period is taken as the  
608 time between easterly and westerly wind transitions at 20 hPa. The simulation produces about 12 QBO  
609 cycles from 1980 to 2005. The average period is 24.6 months, whereas the shortest and longest cycles  
610 last for 18 and 35 months, respectively. ERA-Interim values are 27.9, 23, and 35 months for average,  
611 minimum, and maximum of cycle length. The observed asymmetry in amplitude with the easterlies  
612 being stronger than the westerlies is reproduced in the simulated zonal winds. At 20 hPa, the simulated  
613 easterlies often exceed  $-20 \text{ m s}^{-1}$ , while in the reanalysis easterly winds peak at  $-30$  to  $-40 \text{ m s}^{-1}$ .  
614 Simulated westerlies of the QBO range from 8 to  $12 \text{ m s}^{-1}$ , whereas the reanalysis shows peak winds of  
615 16 to  $20 \text{ m s}^{-1}$ . The amplitudes of the QBO cycles in the simulation are weaker than in the reanalysis,  
616 which is possibly due to inadequate gravity wave forcing to drive the QBO. ~~We suspect that The~~  
617 wave-mean flow interaction based on resolved waves such as Kelvin waves and mixed Rossby-gravity  
618 waves is probably not realistic performant enough in BCC-CSM2-MR. One reason that would contribute  
619 to such a deficiency discrepancy is the relatively coarse vertical resolution (Table 1) that would affect  
620 the vertical wave lengths and the wave damping process. The downward propagation of the simulated  
621 QBO phases occurs in a regular manner, but does not penetrate to sufficiently low altitudes. It may  
622 depend on the vertical resolution and the impact of vertical resolution on downward propagation will be  
623 discussed in a separate paper. After a few test of model vertical layers, we tend to conclude that 46

624 vertical layers (Figure 1) seem the minimum number to simulate QBO in BCC-CSM2-MR. In  
625 BCC-CSM1.1m, however, as shown in Figure 10c, QBO is inexistent and only a semiannual oscillation  
626 of easterlies can be found.

627 Madden-Julian Oscillation (MJO) is a very important atmospheric variability acting within a  
628 periodicity between 20 and 100 days in the tropics with considerable effects on regional weather and  
629 climate. It exerts significant impacts on monsoonal circulations and organization of tropical rainfalls.  
630 From the tropical Indian Ocean to the Western Pacific, MJO shows a pronounced behavior of eastward  
631 propagation, as shown in Figure 11a, in the form of longitude-time, the lagged correlation coefficient of  
632 the rainfall in the eastern Indian Ocean (75–85 °E; 5 °S–5 °N) with other positions and with lagged time.  
633 We can easily observe the eastward-propagating characteristic, with a moving velocity estimated at 5  
634 m s<sup>-1</sup>. As shown in a comparison work of Jiang et al. (2015), three fourth of CMIP5 models don't show  
635 the propagation behavior, with only a standing oscillation when data are filtered to retain only the  
636 20-100 day variability. Figure 11b and 11c show the same plot, but from our two models in CMIP5 and  
637 CMIP6. Although the new model is far from realistic in terms of eastward propagation, there is indeed a  
638 clear improvement compared to the old one.

639 MJO can also exert impacts on weather and climate of extra-tropics, either through emanation of  
640 Rossby waves, or the poleward propagation of MJO itself. Figure 11d shows a latitude-time diagram for  
641 lagged correlation coefficients when rainfalls are filtered to only retain the variability of 20-100 days.  
642 Panels e and f in Figure 11 are the counterpart simulated by our two models. The new model presents a  
643 clear improvement.

#### 644 **4.5 Interannual variation of sea surface temperature (SST) in the equatorial Pacific**

645 Figure 12 shows the observed and simulated spatial pattern of standard deviation of SST anomalies  
646 in the tropical Pacific. Both BCC-CSM2-MR and BCC-CSM1.1m can simulate the position of the  
647 strongest variation of SST, situated in the central-eastern Pacific in the east of the dateline. However,  
648 cold SST in the eastern equatorial Pacific still extends too far west in both models and a cold tongue  
649 bias exists in the equatorial Pacific and even gets a little worse in BCC-CSM2-MR(not shown). The  
650 annual mean SST in the coldest center near 110 °W in the equatorial Pacific reaches below 23°C in  
651 BCC-CSM2-MR, a deterioration compared to-and-colder-than-that-in BCC-CSM1.1m. As shown in

652 Figure 12a, HadISST observations (Rayner et al., 2003) can clearly identify a zone of large interannual  
653 variation of SST from the Peruvian coast to the equatorial cold tongue. It is well simulated in  
654 BCC-CSM2-MR, but almost missing in BCC-CSM1.1m.

655 Figure 13 presents time series of the monthly Nino3.4 SST Index from observations and from  
656 simulations of BCC-CSM1.1m and BCC-CSM2-MR. Although amplitudes of interannual variations of  
657 the Nino3.4 index in both models are larger than in HadISST observations, it gets weaker in  
658 BCC-CSM2-MR with standard deviation of 0.91°C which is close to observation showing standard  
659 deviation of 0.79°C. Recent studies of Lu and Ren (2016) reveal that the mean period ENSO ~~periodicity~~  
660 in BCC-CSM1.1m is only 2.4 years, much shorter than that in observation. This bias of a too-short  
661 periodicity of the ENSO cycle still persists in BCC-CSM2-MR. Nevertheless, The characteristic of  
662 ENSO irregularity is improved in BCC-CSM2-MR in comparison to BCC-CSM1.1m. Lu and Ren  
663 (2016) furthermore pointed out that this ENSO periodicity bias in BCC-CSM1.1m is likely caused by  
664 an underestimated air sea coupling strength, and consequently too weak response of the equatorial  
665 Pacific surface westerly wind to SST warm phase in the eastern Pacific. This can affect and distort the  
666 zonal advective feedback and thermocline feedback which are two crucial mechanisms for the phase  
667 transition of ENSO.

#### 668 **4.6 Sea ice state and oceanic overturning circulation**

669 Figure 14 shows time-series of minimum sea-ice extent from 1851 to 2012 for (a) the Arctic in  
670 September and (b) the Antarctic in March as simulated in BCC-CSM2-MR and BCC-CSM1.1m. Base  
671 on Hadley Centre Sea Ice and Sea Surface Temperature data set (Rayner et al., 2003, shown by “Hadley”  
672 in Figure 14), the observed minimum sea-ice extent in each September from 1851 to 2012 gradually  
673 shrinks, especially since the 1960’s, as caused by global warming (Figure 4). The extent of Arctic sea  
674 ice in September in BCC-CSM1.1m is about  $2 \times 10^6 \text{ km}^2$  ~~less~~ smaller than the Hadley Centre data, and it  
675 early begins to shrink since the 1910’s, earlier than in observations. Although the Arctic sea-ice extent  
676 in September in BCC-CSM2-MR is even ~~less~~ further smaller than ~~the~~ BCC-CSM1.1m simulation, but  
677 this the model bias performance is improved since the 1960’s and ~~much~~ becomes closer to the Hadley  
678 observation. As the NSIDC data we have are from 1979 to 2010, which are not long enough to meet our  
679 needs here, observation based HadISST sea ice data, instead of NSIDC data, are plotted when available,

带格式的：上标

680 ~~where sea ice extent are computed from sea ice concentration. The Arctic sea ice extent in~~  
681 ~~BCC-CSM2-MR is slightly improved, in comparison to BCC-CSM1.1m. But~~ In Figure 14b, it is ~~to be~~  
682 ~~noted that~~ the Antarctic minimum sea-ice extent in the new model is very small, almost a ~~half~~  
683 what observed. The old model had however a more realistic behavior for this regard. This discrepancy  
684 is related to too-warm temperatures simulated in BCC-CSM2-MR in the Southern Ocean, in particular  
685 in the Weddell Sea. The downward trend in the Arctic summer sea-ice extent is, however, better  
686 simulated in the new model than in the old one.

687 Figure 15 shows the seasonal cycle of sea ice extent (SIE) and thickness ~~averaged for the period of~~  
688 ~~1980 to 2005~~ in the two Polar Regions in our models. Observations ~~of from sea ice extent the National~~  
689 ~~Snow and Ice Data Center (NSIDC) and from the Hadley Centre datae~~r and sea ice thickness from the  
690 European Centre for Medium-Range Weather Forecasts (ECMWF) are also plotted for the purpose of  
691 comparison. Observations ~~from NSIDC~~ show that ~~the~~ Arctic sea ice cover reaches a minimum extent of  
692 ~~6.97.74~~ $\times 10^6$  km<sup>2</sup> in September and rises to a maximum extent of ~~16.05.79~~ $\times 10^6$  km<sup>2</sup> in March (Fig. 15a).  
693 The two models can both capture the seasonal variation and pattern, but large biases ~~in BCC-CSM1.1m~~  
694 exist in magnitude, especially in boreal winter, ~~which is evidently improved in BCC-CSM2-MR~~. As  
695 ~~for~~ the Antarctic SIE (Fig. 15b), the ice covers ~~in two models also~~ undergoes a very large seasonal cycle,  
696 which is similar to observations. However, ~~the~~-SIE in BCC-CSM1.1m is too extensive ~~nearly~~  
697 throughout the year, particularly in southern hemisphere winter. Comparatively, the new model  
698 BCC-CSM2-MR simulates a relatively smaller seasonal cycle ~~than that in BCC-CSM1.1m and reduced ice~~  
699 ~~cover in all months, which is and~~ closer to observations ~~except in February to March~~. ~~As to~~In terms of  
700 ice thickness (Fig. 15c and d), the two models simulate a thinner ice cover compared to observations in  
701 all seasons for both ~~the~~ Arctic and Antarctic. ~~—~~The most remarkable improvements of BCC-CSM2-MR  
702 appear ~~in the Arctic~~ in the boreal warm seasons, especially from June to September with thicker ice  
703 presented in the Arctic Ocean. ~~—~~Those improvements may be partly achieved with the new model  
704 physics such as schemes for turbulent flux over sea ice and ocean surfaces, cloud fraction, or  
705 atmospheric circulation improvements at high latitudes. ~~But in the Antarctic, the ice thickness in~~  
706 ~~BCC-CSM2-MR gets worse and even much thinner than that in BCC-CSM1.1m in almost all the year.~~

707 The Atlantic Meridional Overturning Circulation (AMOC) plays a significant role in driving the

708 global climate variation (Caesar et al., 2018). AMOC consists of two primary overturning cells. In the  
709 upper cell, warm water flows northward in the upper 1000 m to supply the formation of the North  
710 Atlantic Deep Water (NADW), which returns southward in the depth range of approximately 1500 to  
711 4000 m. In contrast, in the lower cell, the Antarctic Bottom Water (AABW) flows northward in the  
712 Atlantic basin beneath NADW. Figure 16 shows the time-averaged AMOC simulated by the two  
713 coupled model versions. The two main cells are well depicted. The lower branch of NADW is much  
714 deeper in BCC-CSM2-MR than in BCC-CSM1.1m, as indicated by the depth of the zero-contour line.  
715 Moreover, the central intensity of NADW in BCC-CSM2-MR is over 22.5 Sv about 2.5 Sv stronger  
716 than that in BCC-CSM1.1m, close to observation-based value (25 Sv in Talley et al., 2013).

#### 717 **4.7 Evaluation of models for their performance in East Asia**

718 A good simulation of climate over East Asia is always a challenging issue for the climate modelling  
719 community, as the region is under influences of complex topography (high Tibetan Plateau), and  
720 atmospheric circulations from low latitudes (tropical monsoon circulation) and from higher latitudes.  
721 Figure 17 plots a Taylor diagram to show models performance of main climate variables over East Asia  
722 covering the region (100 °-140 °E, 20 °-50 °N). Both BCC-CSM1.1m (blue figures) and BCC-CSM2-MR  
723 (red figures) are plotted for precipitation, sea-level pressure and variables of the atmospheric general  
724 circulation. There is a clear and remarkable improvement from CMIP5 to CMIP6 in BCC models. The  
725 amelioration is both in the spatial pattern correlation (radial lines) and in the ratio of standard deviations  
726 (circles from the origin).

727 Figure 18 shows the 1980-2005 climatology of December-January-February and June-July-August  
728 averaged precipitation over China and its surroundings. In boreal winter, GPCP precipitations show a  
729 rain belt from Southeast China to Japan and another rain belt along the southwestern flank of the  
730 Tibetan Plateau. In BCC-CSM1.1m the winter precipitation is too weak in Southeast China and too  
731 strong near Japan, compared to GPCP observations. This rain belt in BCC-CSM2-MR obviously  
732 spreads westward and is much closer to observations. The rain belt along the southwestern flank of the  
733 Tibetan Plateau in BCC-CSM2-MR, however, gets too strong. In boreal summer, large dry biases over  
734 East China are present in BCC-CSM1.1m. Those biases are reduced in BCC-CSM2-MR. The center of  
735 precipitation around Japan is also well simulated in BCC-CSM2-MR.

736 The East Asian summer monsoon rainfall has a seasonal progression from south to north at the  
737 beginning of summer and then a quick retreat to the south when the summer monsoon terminates (as  
738 shown in Figure 19a). This phenomenon is strongly related to the fact that the East Asian monsoon  
739 rainfall mainly takes place in the frontal zone between warm and humid air mass from the south, and  
740 cold and dry air mass from the north. This seasonal migration is also accompanied with a meridional  
741 movement of the Western North Pacific Subtropical High, an important atmospheric center of action  
742 controlling the climate of the region. In Figure 19 (panels b and c), we compare the two models in terms  
743 of seasonal migration of the monsoon rainfall. In the old model, rainfall was too weak. The new model  
744 produces more precipitation. In terms of seasonal match, both models show a delay of the peak rainfall  
745 by about one month, even longer in BCC-CSM2-MR.

746 Finally, let us examine the rainfall diurnal cycle in summer. Figure 20 shows the timing of the  
747 rainfall diurnal cycle from observation and the two models. Main zones of nocturne rainfall can be  
748 recognized in the south flank of the Tibetan Plateau, in the Sichuan Basin in the east of the Tibetan  
749 Plateau, and in the north of Xinjiang in Central Asia. There is also a zone of nocturne rainfall in the low  
750 reach of the Yellow River. This is mainly under the influence of nocturne rainfall in the area of the  
751 Bohai Sea. Other regions over land experience diurnal rainfall peak in the afternoon after 16 hours local  
752 time. The diurnal cycle of rainfall was extensively studied in Jin et al. (2013) in terms of physics  
753 causing the diurnal cycle. But the good simulation of diurnal cycle is always a major challenge for  
754 climate modeling. We can see that it is not very well simulated in our old model and in East China the  
755 peak occurs in the mid and later night (0-4 am). But the improvement is quite spectacular in our new  
756 model with rainfall peak delayed in the afternoon. Such an improvement is due to the implementation of  
757 our new trigger scheme in convection parameterization.

## 758 **5. Conclusions and discussion**

759 This paper presents the main progress of BCC climate system models from CMIP5 to CMIP6 and  
760 focuses on the description of CMIP6 version BCC-CSM2-MR and CMIP5 version BCC-CSM1.1m  
761 especially on the model physics. Main updates in model physics include a modification of deep  
762 convection parameterization, a new scheme for cloud fraction, indirect effects of aerosols through  
763 clouds and precipitation, and the gravity wave drag generated by deep convection. Surface processes in

764 BCC-AVIM have also been significantly improved for soil water freezing treatment, snow aging effect  
765 on surface albedo, and timing of vegetation leaf unfolding, growth, and withering. A four-stream  
766 radiation transfer within the vegetation canopy replaced the two-stream radiation transfer. There is a  
767 new treatment for rice paddy waters. New schemes for surface turbulent fluxes of momentum, heat and  
768 water at the interface of atmosphere and sea/sea ice are also used.

769 The evaluation of model performance in simulating present-day climatology is presented for main  
770 climate variables, such as, surface air temperature, precipitation, and atmospheric circulation for the  
771 globe and for East Asia. Emphasis is put on comparison between the CMIP5 and CMIP6 model  
772 versions (BCC-CSM2-MR versus BCC-CSM1.1m). The globally-averaged TOA net energy budget is  
773  $0.85 \text{ W} \cdot \text{m}^{-2}$  in BCC-CSM2-MR, and  $0.98 \text{ W} \cdot \text{m}^{-2}$  in BCC-CSM1.1m. Both versions have a very good  
774 energy equilibrium. Model biases of excessive cloud shortwave and longwave radiative forcings over  
775 low latitudes in BCC-CSM1.1m are obviously reduced in BCC-CSM2-MR. When Taylor diagrams are  
776 used to compare the two models for spatial patterns of main climate variables such as 2-meter surface  
777 air temperature, precipitation, and atmospheric general circulation, BCC-CSM2-MR shows an overall  
778 improvement at both global scale and regional scale in East Asia. These improvements in  
779 BCC-CSM2-MR are believed to be achieved by the new scheme of cloud fraction and by the  
780 consideration of indirect effects of aerosol on clouds and precipitation. The cold tongue bias of SST in  
781 the equatorial Pacific in BCC-CSM1.1m still exists in BCC-CSM2-MR. BCC-CSM1.1m has a severe  
782 bias in sea ice extent (SIE) and thickness (Tan et al., 2015): too extensive in cold seasons and less  
783 extensive in warm seasons in both hemispheres. The most impressive improvements in  
784 BCC-CSM2-MR appear in the boreal warm seasons, especially from June to September with thicker ice  
785 presented in the Arctic Ocean. However, in the Southern Hemisphere, the sea ice extent and thickness in  
786 BCC-CSM2-MR become even smaller than those in its previous version. This is still an issue that needs  
787 to be addressed in our future work. There is another model bias of weak oceanic overturning circulation  
788 in BCC-CSM1.1m. This bias is reduced in the new version BCC-CSM2-MR, and the strength of  
789 AMOC is increased.

790 Further evaluations are performed on climate variabilities at different time scales, including  
791 long-term trend of global warming in the 20<sup>th</sup> century, QBO, MJO, and diurnal cycle of precipitation.

792 The globally-averaged annual-mean surface air temperature from the historical simulation of  
793 BCC-CSM2-MR is much closer to HadCRUT4 observation than BCC-CSM1.1m, and the observed  
794 global warming hiatus or warming slowdown in the period from 1998 to 2013 is captured in some  
795 realization of BCC-CSM2-MR. With a higher vertical resolution and inclusion of the gravity wave drag  
796 generated by deep convection, the new version BCC-CSM2-MR is able to reproduce the stratospheric  
797 QBO, while QBO even does not exist in BCC-CSM1.1m. Further investigations on physical  
798 mechanisms controlling QBO simulation in BCC-CSM2-MR will be reported in future. MJO is a very  
799 important atmospheric oscillation at intra-seasonal scales and main features are reproduced and  
800 improved in BCC-CSM2-MR, but with intensity still weaker than its counterpart in observation. At  
801 interannual scale, BCC-CSM1.1m shows too-strong variations of Nino 3.4 SST index, but too-short and  
802 too-regular periodicity for ENSO. BCC-CSM2-MR shows weaker amplitude for Nino 3.4 SST index,  
803 which is an improvement and closer to HadISST observations. The rainfall diurnal cycle in China has  
804 strong regional variations with pronounced nocturne rainfalls in the Sichuan Basin and in north China  
805 near the Bohai Sea and the coast. The diurnal rainfall generally peaks in the local time afternoon for  
806 most other land regions. BCC-CSM2-MR shows a clear improvement of rainfall diurnal peaks  
807 compared to the CMIP5 model (BCC-CSM1.1m). This improvement of rainfall diurnal variation is  
808 strongly related to the modification of deep convection scheme.

809 Finally, we also evaluate the climate sensitivity to CO<sub>2</sub> increasing in the standard simulation of 1%  
810 CO<sub>2</sub> increase per year (1pctCO<sub>2</sub>) and the 4xCO<sub>2</sub> abrupt-change. The transient climate response in the  
811 new CMIP6 model version BCC-CSM2-MR is lower than that in the previous CMIP5 model  
812 BCC-CSM1.1m, while the equilibrium climate sensitivity ECS for BCC-CSM2-MR is slightly higher  
813 than its counterpart in BCC-CSM1.1m.

814 From our model evaluations, we find that although basic feature of the QBO can be simulated in  
815 BCC-CSM2-MR, the magnitude between westerly and easterly interchange is still too weak. We also  
816 note that there are large biases of air temperature and winds in the stratosphere. Therefore, improvement  
817 of the stratospheric temperature and circulation simulations is an important priority in the future  
818 development of BCC models. In addition, sea ice simulation in the Antarctic region has large biases,  
819 which need to be improved.

820 **6. Code and data availability**

821 Source codes of BCC models are freely available upon request addressed to Tongwen Wu  
822 (twwu@cma.gov.cn). Model output of BCC models for both CMIP5 and CMIP6 simulations described  
823 in this paper is distributed through the Earth System Grid Federation (ESGF) and freely accessible  
824 through the ESGF data portals after registration. Details about ESGF are presented on the CMIP Panel  
825 website at <http://www.wcrp-climate.org/index.php/wgcm-cmip/about-cmip>.

826  
827 **Author contributions**

828 Tongwen Wu led the BCC-CSM development. Tongwen Wu and Xiaoge Xin designed the experiments  
829 and carried them out. Tongwen Wu, Laurent Li, and Xiaohong Liu wrote the final document with  
830 contributions from all other authors.

831  
832 **Acknowledgements**

833 This work was supported by The National Key Research and Development Program of China  
834 (2016YFA0602100). [Two anonymous reviewers are acknowledged for their constructive comments on](#)  
835 [earlier versions of the paper.](#)

836 **References**

- 837 Albrecht, B.: Aerosols, cloud microphysics, and fractional cloudiness, *Science*, 245, 1227–1230, 1989.
- 838 Adler, R. F., Chang, A.: The Version 2 Global Precipitation Climatology Project (GPCP) Monthly Precipitation  
839 Analysis (1979-Present), *J. Hydrometeor.*, 4, 1147–1167, 2003
- 840 Alexander, M. J., May, P. T., and Beres, J. H.: Gravity waves generated by convection in the Darwin area during  
841 the Darwin Area Wave Experiment, *J. Geophys. Res.*, 109, D20S04, doi: 10.1029/2004JD004729, 2004.
- 842 Allen, M., Stott, P., Mitchell, J., Schnur, R., and Delworth, T.: Quantifying the uncertainty in forecasts of  
843 anthropogenic climate change, *Nature*, 407, 617-620, 2000.
- 844 Arora, V. K., and Boer, G. J.: A parameterization of leaf phenology for the terrestrial ecosystem component of  
845 climate models, *Global Change Biology*, 11, 39-59, doi:10.1111/j.1365-2486.2004.00890.x, 2005.
- 846 Andreas, E. L.: A theory for the scalar roughness and the scalar transfer coefficients over snow and sea ice,  
847 *Bound.-Layer Meteor.*, 38, 159-184, 1987.
- 848 Andreas, E. L.: Parameterizing scalar transfer over snow and ice: A review, *Journal of Hydrometeorology*, 3,

849 417-432, 2002.

850 Andreas, E. L., Horst, T. W., Grachev, A. A., Persson, P. O. G., Fairall, C. W., and Guest, P. S., and Jordan, R.E.:  
851 Parametrizing turbulent exchange over summer sea ice and the marginal ice zone, *Quarterly Journal of the*  
852 *Royal Meteorological Society*, 136, 927-943, 2010a.

853 Andreas, E. L., Persson, P. G., Jordan, R. E., Horst, T.W., Guest, T.S., Grachev, A.A., and Fairall, C.W.:  
854 Parameterizing turbulent exchange over sea ice in winter, *Journal of Hydrometeorology*, 11, 87-104, 2010b.

855 Andrews, T., Gregory, J. M., Webb, M. J., and, K. E.: Forcing, feedbacks and climate sensitivity in CMIP5  
856 coupled atmosphere-ocean climate models, *Geophys. Res. Lett.*, 38, L09712, doi: 10.1029/2012GL051607,  
857 2012.

858 Beres, J. H., Alexander, M. J., and Holton, J. R.: A method of specifying the gravity wave spectrum above  
859 convection based on latent heating properties and background wind, *J. Atmos. Sci.*, 61, 324-337, 2004.

860 Boucher, O., Lohmann, U.: The sulphate-CCN-cloud albedo effect – a sensitivity study with two general  
861 circulation models, *Tellus* 47B, 281–300, 1995.

862 Caesar, L., Rahmstorf, S., Robinson, A., Feulner, G., Saba, V.: Observed fingerprint of a weakening Atlantic  
863 Ocean overturning circulation, *Nature*, 556, 191-196, 2018.

864 Campin J.M., and Goosse, H.: Parameterization of density-driven downsloping flow for a coarse-resolution ocean  
865 model in z-coordinate, *Tellus*, 51A, 412–430, 1999.

866 Cao M., and Woodward F. I.: Net primary and ecosystem production and carbon stocks of terrestrial ecosystems  
867 and their responses to climate change, *Global Change Biology*, 4, 185-198, 1998.

868 Chen C., and Cotton, W. R.: The physics of the marine stratocumulus-capped mixed layer, *J. Atmos. Sci.*, 44 (50),  
869 2951–2977, 1987.

870 Chen A., Li, W. P., Li, W. J., and Liu, X.: An observational study of snow aging and the seasonal variation of  
871 snow albedo by using data from Col de Porte, France. *Chinese Science Bulletin*, 59 (34), 4881-4889, 2014

872 Collins, W. D., Rasch, P.J., Boville, B.A., Hack, J. J., McCaa, J.R., Williamson, D. L., Kiehl, J. T., Briegleb, B.,  
873 Bitz C., Lin S.J., Zhang, M.H., and Dai, Y.J.: Description of the NCAR community atmosphere model  
874 (CAM3). Technical Report NCAR/TN-464 + STR, National Center for Atmospheric Research, Boulder,  
875 Colorado, 226 pp, 2004.

876 Collins, W. J., Lamarque, J.-F., Schulz, M., Boucher, O., Eyring, V., Hegglin, M. I., Maycock, A., Myhre, G.,  
877 Prather, M., Shindell, D., and Smith, S. J.: AerChemMIP: quantifying the effects of chemistry and aerosols  
878 in CMIP6, *Geosci. Model Dev.*, 10, 585–607, 2017.

879 Danabasoglu, G., and Co-authors: North Atlantic simulations in Coordinated Ocean-ice Reference  
880 Experiments phase II (CORE-II). Part I: Mean States. *Ocean Modelling*, 73, 76-107, doi:  
881 10.1016/j.ocemod.2013.10.005, 2014.

882 Dee, D.P., Uppala, S. M., Simmons, A. J., Berrisford, P., Poli, P., Kobayashi, S., Andrae, U., Balmaseda, M. A.,  
883 Balsamo, G., Bauer, P., Bechtold, P., Beljaars, A. C. M., Berg L., Bidlot, J., Bormann, N., Delsol, C., Dragani,  
884 R., Fuentes, M., Geer, A. J., Haimberger, L., Healy, S. B., Hersbach, H., Holm, E. V., Isaksen, L., Kallberg, P.,  
885 Kohler, M., Matricardi, M., McNally, A.P., Monge-Sanz, B. M., Morcrette, J.-J., Park, B.-K., Peubey, C.,  
886 Rosnay, P., Tavolato, C., Thepaut, J.-N., and Vitart F.: The ERA-Interim reanalysis: configuration and  
887 performance of the data assimilation system, *Quart. J. R. Meteorol. Soc.*, 137, 553-597 (DOI:  
888 10.1002/qj.828), 2011.

889 Ding, Y. H., Liu, Y. M., Song, Y. J., Li, Q. Q.: Research and experiments of the dynamical model system for  
890 short-term climate prediction, *Climatic Environ. Res.*, 7(2), 236–246, 2002 (in Chinese).

891 Eyring, V., Bony, S., Meehl, G. A., Senior, C. A., Stevens, B., Stouffer, R. J., Taylor, K. E.: Overview of the  
892 Coupled Model Intercomparison Project Phase 6 (CMIP6) experimental design and organization, *Geosci.*  
893 *Model Dev.*, 9, 1937–1958, 2016, 2017.

894 Fetterer, F., Knowles, K., Meier, W., Savoie, M.: Sea Ice Index, digital media, National Snow and Ice Data Center.  
895 Boulder, CO., 2002.

896 Fyfe, J.C., Meehl, G.A., England, M.H., Mann, M. E. Santer, B. D., Flato, G. M., Hawkins, E., Gillett, N. P., Xie,  
897 S.-P., Kosaka, Y., Swart, N. C.: Making sense of the early-2000s warming slowdown, *Nat. Clim. Change* 6,  
898 224–228, 2016.

899 Griffies, S. M., Gnanadesikan, A., Dixon, K. W., Dunne, J. P., Gerdes, R., Harrison, M. J., Rosati, A., Lin, J.,  
900 Bonita, R., Samuels, L., Spelman, M. J., Winton, M., Zhang, R.J.: Formulation of an ocean model for  
901 global climate simulations, *Ocean Sci.*, 1, 45–79, 2005.

902 Gregory, J. M., Ingram, W. J., Palmer, M. A., Jones, G. S., Stott, P. A., Thorpe, R. B., Lowe, J. A., Johns, T. C.,  
903 and Williams, K. D.: A new method for diagnosing radiative forcing and climate sensitivity, *Geophys. Res.*  
904 *Lett.*, 31, L03205, doi:10.1029/2003GL018747, 2004.

905 Gregory, J.M., Webb, M. J., and Taylor, K. E.: Forcing, feedbacks and climate sensitivity in CMIP5 coupled  
906 atmosphere-ocean climate models, *Geophys. Res. Lett.*, 39, L09712, doi:10.1029/2012GL051607, 2012.

907 Gent, P. R., McWilliams, J. C.: Isopycnal mixing in ocean circulation Models[J]. *Journal of Physical*  
908 *Oceanography*, 20(1), 150–155, 1990.

909 Guenther, A. B., Jiang, X., Heald, C. L., Sakulyanontvittaya, T., Duhl, T., Emmons, L. K., and Wang, X.: The  
910 Model of Emissions of Gases and Aerosols from Nature Version 2.1 (MEGAN2.1): An Extended and  
911 Updated Framework for Modeling Biogenic Emissions, *Geoscientific Model Development* 5(6): 1471–1492,  
912 2012.

913 Hack, J. J., Parameterization of moist convection in the National Center for Atmospheric Research Community  
914 Climate Model (CCM2), *J. Geophys. Res.*, 99, 5551–5568, 1994.

915 Haarsma, R. J., Roberts, M. J., Vidale, P. L., Senior, C. A., Bellucci, A., Bao, Q., Chang, P., Corti, S., Fuckar, N.  
916 S., Guemas, V., Hardenberg, J. von, Hazeleger, W., Kodama, C., Koenigk, T., Leung, L. R., Lu, J., Luo, J. –J.,  
917 Mao, J., Mizielinski, M. S., Mizuta, R. Nobre, P., Satoh, M., Scoccimarro, E., Semmler, T., Small, J., and  
918 Storch, J.–S. von : High Resolution Model Intercomparison Project (HighResMIP v1.0) for CMIP6, *Geosci.*  
919 *Model Dev.*, 9, 4185–4208, doi:10.5194/gmd-9-4185-2016, 2016.

920 Holtslag, A. A. M., and Boville, B. A.: Local versus nonlocal boundary-layer diffusion in a global climate model,  
921 *J. Climate*, 6, 1825–1842, 1993.

922 Huffman, G., Bolvin, D., Braithwaite, D., Hsu, K., Joyce, R., Xie, P.: Integrated Multi-satellitE Retrievals for  
923 GPM (IMERG), version 4.4. NASA's Precipitation Processing Center, accessed 31 March, 2015,  
924 <ftp://arthurhou.pps.eosdis.nasa.gov/gpmpdata/>, 2014.

925 IPCC Climate Change: The Physical Science Basis (eds Stocker, T. F., Qin, D., Plattner, G.-K., Tignor, M., Allen,  
926 S. K., Boschung, J., Nauels, A., Xia, Y., Bex V., and Midgley, P. M.) , Cambridge Univ. Press, Cambridge,  
927 United Kingdom and New York, NY, USA, 2013.

928 Ji, J.: A climate-vegetation interaction model: Simulating physical and biological processes at the surface, *Journal*  
929 *of Biogeography*, 22, 2063-2069, 1995.

930 Ji, J., Huang, M., and Li, K.: Prediction of carbon exchange between China terrestrial ecosystem and atmosphere  
931 in 21st century, *Sci. China Ser. D: Earth Sci.*, 51(6), 885-898, 2008.

932 Li, J. D., Wang, W.-C., Liao, H., and Chang, W. Y.: Past and future direct radiative forcing of nitrate aerosol in  
933 East Asia, *Theoretical and Applied Climatology*, 121, 445-458, 2015.

934 Lu, B., Ren, H.-L.: Improving ENSO periodicity simulation by adjusting cumulus entrainment in BCC\_CSMs,  
935 *Dynamics of Atmospheres and Oceans*, 76, 127-140, 2016.

936 Jiang X., Waliser, D. E. Xavier, P.K., Petch, J., Klingaman, N. P., Woolnough, S.J., Guan, B., Bellon, G., Crueger,  
937 T., DeMott, C., Hannay, C., Lin, H., Hu, W., Kim, D., Lappen, C., Lu, M.-M., Ma, H.-Y., Miyakawa, T.,  
938 Ridout, J. A., Schubert, S.D., Scinocca, J., Seo, K.-H., Shindo, E., Song, X., Stan, C., Tseng, W.-L., Wang,

939 W., Wu, T., Wyser, K., Wu, X., Zhang, G. J., Zhu, H.: Exploring Key Processes of the Madden-Julian  
940 Oscillation (MJO): A Joint WGNE MJO Task Force / GEWEX GASS Project on the Vertical Structure and  
941 Diabatic Processes of the MJO – Part I. Climate Simulations, *J. Geophys. Res. Atmos.*, 120, 4718–4748.  
942 doi:10.1002/2014JD022375, 2015.

943 Jin, X., Wu, T., Li, L.: The quasi-stationary feature of nocturnal precipitation in the Sichuan Basin and the role of  
944 the Tibetan Plateau, *Climate Dynamics*, 41: 977-994. DOI: 10.1007/s00382-012-1521-y, 2013.

945 Jones, C.D., Arora, V., Friedlingstein, P., Bopp, L., Brovkin, V., Dunne, J., Graven, H., Hoffman, F., Ilyina, T.,  
946 John, J. G., Jung, M., Kawamiya, M., Koven, C., Pongratz, J., Raddatz, T., Randerson, J. T., and Zaehele, S.:  
947 C4MIP – The Coupled Climate–Carbon Cycle Model Intercomparison Project: experimental protocol for  
948 CMIP6, *Geosci. Model Dev.*, 9, 2853–2880, doi:10.5194/gmd-9-2853-2016, 2016.

949 Klein, S. A., and Hartmann, D. L.: The seasonal cycle of low stratiform clouds, *J. Climate*, 6, 1587–1606, 1993.

950 Kristjánsson, J. E., Edwards, J. M., Mitchell, D. L.: Impact of a new scheme for optical properties of ice crystals  
951 on climates of two GCMs, *J. Geophys. Res.*, 105(D8), 10063–10079, doi:10.1029/2000JD900015, 2000.

952 Lamarque, J.-F., Emmons, L. K., Hess, P. G., Kinnison, D. E., Tilmes, S., Vitt, F., Heald, C. L., Holland, E. A.,  
953 Lauritzen, P. H., Neu, J., Orlando, J. J., Rasch, P. J., and Tyndall, G. K.: CAM-chem: description and  
954 evaluation of interactive atmospheric chemistry in the Community Earth System Model, *Geosci Model Dev.*,  
955 5, 369-411, 2012.

956 Large, W. G., McWilliams, J. C., and Doney, S. C.: Oceanic vertical mixing: A review and a model with a  
957 nonlocal boundary layer parameterization, *Rev. Geophys.*, 32, 363-403, 1994.

958 Liu, Y., and Daum, P. H.: Indirect warming effect from dispersion forcing, *Nature*, 419, 580-581, 2002.

959 Liou, K. N.: An Introduction to Atmospheric Radiation, China Meteorological Press, 313-327 (in Chinese), 2004.

960 Loeb, N.G., Lyman, J.M., Johnson, G.C., Allan, R.P., Doelling, D.R., Wong, T., Soden, B.J., and Stephens, G.L.:  
961 Observed changes in top-of-the-atmosphere radiation and upper-ocean heating consistent within uncertainty,  
962 *Nature Geosciences*, DOI 10.1038/NGE, 2012.

963 Lu, Y., Zhou, M., and Wu, T.: Validation of parameterizations for the surface turbulent fluxes over sea ice with  
964 CHINARE 2010 and SHEBA data, *Polar Research*, 32, 20818, <http://dx.doi.org/10.3402/polar.v32i0.20818>,  
965 2013.

966 Meehl, G.A., Boer, G.J., Covey, C., Latif, M., Stouffer, R.J.: Intercomparison makes for a better climate model.  
967 *Eos, Trans.Amer.Geophys.Union*, 78, 445–451, doi:10.1029/97EO00276.

968 Medhaug, I., Martin, B. S., Erich, M. F., and Knutti, R.: Reconciling controversies about the ‘global warming

969 hiatus', *Nature*, 545, 41–47, 2017.

970 Morice, C. P., Kennedy, J. J., Rayner, N.A., and Jones, P.D.: Quantifying uncertainties in global and regional  
971 temperature change using an ensemble of observational estimates: The HadCRUT4 data set, *J. Geophys. Res.*  
972 117, D08101, 2012.

973 Martin, G.M., Johnson, D.W., and Spice, A.: The measurement and parameterisation of effective radius of  
974 droplets in warm stratocumulus clouds, *J. Atmos. Sci.*, 51, 1823–1842, 1994.

975 McFarlane, N. A.: The effect of orographically excited gravity wave drag on the general circulation of the lower  
976 stratosphere and troposphere, *J. Atmos. Sci.*, 44, 1775-1800, 1987.

977 Oleson, K. W., Lawrence, D. M. and Dai, Y. J.: Technical description of the Community Land Model (CLM),  
978 NCAR Technical Note NCAR/TN-461+STR, 2004.

979 Pontikis, C.A., and Hicks, E.; Contribution to the cloud droplet effective radius parameterization, *Geophys. Res.*  
980 *Lett.* 19, 2227–2230, 1992.

981 Peng, Y., and Lohmann, U.: Sensitivity study of the spectral dispersion of the cloud droplet size distribution on  
982 the indirect aerosol effect, *Geophys. Res. Lett.*, 30(10), 1507, doi:10.1029/2003GL017192, 2003.

983 Quaas J, Boucher O, and Lohmann U: Constraining the total aerosol indirect effect in the LMDZ and ECHAM4  
984 GCMs using MODIS satellite data. *Atmos Chem Phys* 6,947-955, 2006

985 Rasch, P. J., and Kristj ánsson, J. E.: A comparison of the CCM3 model climate using diagnosed and predicted  
986 condensate parameterizations, *J. Climate*, 11, 1587-1614, 1998.

987 Rahmstorf, S.: A fast and complete convection scheme for ocean models, *Ocean Modelling*, 101, 9–11, 1993.

988 Rayner, N. A., Parker, D. E., Horton, E. B., Folland, C., Alexander, L., Rowell, D., Kent, E., and Kaplan, A.:  
989 Global analyses of sea surface temperature, sea ice, and night marine air temperature since the late  
990 nineteenth century, *Journal of Geophysical Research*, 108(D14), 4407, doi:10.1029/2002JD002670, 2003.

991 Richter, J. H., Sassi, F., and Garcia, R. R.: Toward a physically based gravity wave source parameterization in a  
992 general circulation model, *J. Atmos. Sci.*, 67, 136--156, 2010.

993 Sweeney, C., Gnanadesikan, A., Griffies, S. M., Harrison, M., Rosati, A., Samuels, B.: Impacts of shortwave  
994 penetration depth on large-scale ocean circulation and heat transport, *Journal of Physical Oceanography* 35,  
995 1103–1119, 2005.

996 Stevens, B., Fiedler, S., Kinne, S., Peters, K., Rast, S., Musse, J., Smith, S.J., and Mauritsen, T.: MACv2-SP: a  
997 parameterization of anthropogenic aerosol optical properties and an associated Twomey effect for use in  
998 CMIP6, *Geos.Mod.Dev.*,10, 433-452, 2017.

999 Talley, L.D.: Closure of the global overturning circulation through the Indian, Pacific, and Southern Oceans:  
1000 Schematics and transports, *Oceanography*, 26, 80–97, 2013.

1001 Tan, H.H., Zhang, L.J., Chu, M., Wu, T.W., Qiu, B., and Li, J.L.: An analysis of simulated global sea ice extent,  
1002 thickness, and causes of error with the BCC\_CSM model. *Chinese Journal of Atmospheric Sciences (in*  
1003 *Chinese)*, 39 (1): 197–209, 2015.

1004 Taylor, K. E., Stouffer, R. J., and Meehl, G. A.: An Overview of Cmp5 and the Experiment Design, *B. Am.*  
1005 *Meteorol. Soc.*, 93, 485–498, 2012.

1006 Tietsche, S., Balmaseda, M., Zuo, H., Mogensen, K.: Arctic sea ice in the ECMWF MyOcean2 ocean reanalysis  
1007 ORAP5. Tech Rep 737, European Center for Medium-Range Weather Forecasts, Reading, UK, 2014.

1008 Wielicki, B.A., Barkstrom, B. R., Harrison, E. F., Lee, R. B., Smith, G. L., and Cooper, J. E.: Clouds and the  
1009 earth’s radiant energy system (CERES): an earth observing system experiment, *Bull. Am. Meteorol. Soc.*, 77,  
1010 853–868, 1996.

1011 Winton, M.: A reformulated three-layer sea ice model, *J. Atmo.Oceanic Technol.*, 17, 525–531, 2000.

1012 Wu, T., Song, L., Li, W., Wang, Z., Zhang, H., Xin, X., Zhang, Y., Zhang, L., Li, J., Wu, F., Liu, Y., Zhang, F., Shi,  
1013 X., Chu, M., Zhang, J., Fang, Y., Wang, F., Lu, Y., Liu, X., Wei, M., Liu, Q., Zhou, W., Dong, M., Zhao, Q., Ji,  
1014 J., Li, L., and Zhou, M.: An overview of BCC climate system model development and application for  
1015 climate change studies, *J. Meteor. Res.*, 28(1), 34-56, 2014.

1016 Wu, T., Li, W., Ji, J., Xin, X., Li, L., Wang, Z., Zhang, Y., Li, J., Zhang, F., Wei, M., Shi, X., Wu, F., Zhang, L.,  
1017 Chu, M., Jie, W., Liu, Y., Wang, F., Liu, X., Li, Q., Dong, M., Liang, X., Gao, Y., and Zhang, J.: Global  
1018 carbon budgets simulated by the Beijing climate center climate system model for the last century, *J Geophys*  
1019 *Res Atmos*, 118, 4326-4347. doi: 10.1002/jgrd.50320, 2013.

1020 Wu, T.: A Mass-Flux Cumulus Parameterization Scheme for Large-scale Models: Description and Test with  
1021 Observations, *Clim. Dyn.*, 38:725–744, DOI: 10.1007/s00382-011-0995-3, 2012.

1022 Wu, T., Yu, R., Zhang, F., Wang, Z., Dong, M., Wang, L., Jin, X., Chen, D.L., and Li, L.: The Beijing Climate  
1023 Center atmospheric general circulation model: description and its performance for the present-day climate,  
1024 *Climate Dynamics*, 34, 123-147, DOI 10.1007/s00382-008-0487-2, 2010.

1025 Wu, T., Yu, R., and Zhang, F.: A modified dynamic framework for atmospheric spectral model and its application,  
1026 *J. Atmos.Sci.*, 65, 2235-2253, 2008

1027 Wu, T., and Wu, G.: An empirical formula to compute snow cover fraction in GCMs, *Adv.Atmos.Sci.*, 21,  
1028 529-535, 2004.

1029 Xia, K., Luo, Y., and Li, W. P.: Simulation of freezing and melting of soil on the northeast Tibetan Plateau.  
1030 Chinese Sci. Bull., 56, 1-4, doi: 10.1007/s11434-011-4542-8, 2011.

1031 Xin, X., Wu, T., and Zhang, J.: Introduction of CMIP5 experiments carried out with the climate system models of  
1032 Beijing Climate Center, Adv. Clim. Change Res., 4(1), 41-49, doi: 10.3724/SP.J.1248.2013.041, 2013.

1033 Xu, K. M., and Krueger, S. K.: Evaluation of cloudiness parameterizations using a cumulus ensemble model,  
1034 Mon. Wea. Rev., 119, 342–367, 1991.

1035 Xu, L., and Penner, J.E.: Global simulations of nitrate and ammonium aerosols and their radiative effects, Atmos.  
1036 Chem. Phys., 12, 9479-9504, 2012.

1037 Zeng, X., Zhao, M., and Dickinson, R. E.: Intercomparison of bulk aerodynamic algorithms for the computation  
1038 of sea surface fluxes using TOGA COARE and TAO data, J. Climate, 11, 2628-2644, 1998.

1039 Zeng, X., Zhang, Q., Johnson, D., and Tao, W.-K.: Parameterization of wind gustiness for the computation of  
1040 ocean surface fluxes at different spatial scales, Monthly Weather Review, 130, 2125-2133, 2002.

1041 Zhang, G.J.: Convective quasi-equilibrium in midlatitude continental environment and its effect on convective  
1042 parameterization. J Geophys Res 107(D14), doi:10.1029/2001JD001005, 2002.

1043 Zhang, M., Lin, W., Bretherton, C. S., Hack, J. J., and Rasch, P. J.: A modified formulation of fractional  
1044 stratiform condensation rate in the NCAR community atmospheric model CAM2, J. Geophys. Res., 108  
1045 (D1), 2003.

1046 Zhang, Y., Gao, Z., Li, D., Li, Y., Zhang, N., Zhao, X., and Chen, J.: On the computation of planetary  
1047 boundary-layer height using the bulk Richardson number method, Geosci. Model Dev., 7, 2599–2611, 2014.

1048 Zhou, W.Y., Luo, Y., Li, W.P., Shi, X.L., and Zhang, Y: Comparative studies of different radiation schemes within  
1049 vegetation in land model, Chinese Science Bulletin, 63, 10.1360/N972018-00398, 2018.

Table 1. BCC models for CMIP5 and CMIP6

Model versions	Atmosphere	Atmos Chemistry and Aerosol	Land Surface	Ocean	Sea Ice
BCC-CSM1.1 in CMIP5 (Wu et al., 2013)	BCC-AGCM2.1 (1) T42, 26 layers (2) Top at 2.917 hPa	(1) Prescribed aerosols (2) No atmospheric chemistry (3) Global carbon budget without spatial distribution	BCC-AVIM1.0	MOM4-L40v1 (1) Tri-polar: 0.3 to 1 deg latitude x 1 deg longitude, and 40 layers (2) Oceanic carbon cycle based on OCMIP2	SISv1
BCC-CSM1.1m in CMIP5 (Wu et al., 2013)	BCC-AGCM2.2 (1) T106, 26 layers (2) Top at 2.917 hPa	Same as BCC-CSM1.1	BCC-AVIM1.0	MOM4-L40v2	SISv2
BCC-CSM2-MR In CMIP6	BCC-AGCM3-MR (1) T106, 46 layers (2) Top at 1.459 hPa	(1) Prescribed aerosols (2) No atmospheric chemistry (3) Prognostic spatial CO <sub>2</sub> in the atmosphere	BCC-AVIM2.0	MOM4-L40v2	SISv2
BCC-CSM2-HR In CMIP6	BCC-AGCM3-HR (1) T266, 56 layers (2) Top at 0.092 hPa	(1) Prescribed aerosols (2) No atmospheric chemistry	BCC-AVIM2.0	MOM4-L40v2	SISv2
BCC-ESM1 In CMIP6	BCC-AGCM3-Chem (1) T42, 26 layers (2) Top at 2.917 hPa	(1) Prognostic aerosols (2) MOZART2 atmospheric chemistry	BCC-AVIM2.0	MOM4-L40v2	SISv2

Table 2. Main physics schemes in atmospheric components (BCC-AGCM) of BCC-CSM versions for CMIP5 and CMIP6

	<b>BCC-AGCM2 for CMIP5</b>	<b>BCC-AGCM3 for CMIP6</b>
<b>Deep convection</b>	The cumulus convection parameterization scheme (Wu, 2012)	A modified Wu'2012 scheme described in this work
<b>Shallow/Middle Tropospheric Moist Convection</b>	Hack (1994)	Hack (1994)
<b>Cloud macrophysics</b>	Cloud fraction diagnosed from updraft mass flux and relative humidity (Collins et al., 2004)	A new scheme to diagnose cloud fraction described in this work
<b>Cloud microphysics</b>	Modified scheme of Rasch and Kristj ánsson (1998) by Zhang et al. (2003). No aerosol indirect effects	Modified scheme of Rasch and Kristj ánsson (1998) by Zhang et al. (2003), but included the aerosol indirect effects in which liquid cloud droplet number concentration is diagnosed using the aerosols masses.
<b>gravity wave drag</b>	Gravity wave drag only generated by orography (Mcfarlane 1987)	Gravity wave drag generated by both orography (Mcfarlane 1987) and convection (Beres et al., 2004) using tuned parameters related to model resolutions.
<b>Radiative transfer</b>	Radiative transfer scheme used in CAM3 (Collins et al., 2004) with no aerosol indirect effects, and cloud drop effective radius for clouds is only function of temperature and has a distinct difference between maritime, polar, and continental for warm clouds.	Radiative transfer scheme used in CAM3 (Collins et al., 2004), but including the aerosol indirect effects, and the effective radius of the cloud drop for liquid clouds is diagnosed using liquid cloud droplet number concentration.
<b>Boundary Layer</b>	ABL parameterization [Holtslag and Boville, 1993]	ABL parameterization [Holtslag and Boville, 1993], but modified PBL height computation referred to Zhang et al. (2014)

Table 3. Main physics schemes in BCC-AVIM versions

BCC-AVIM1.0 in CMIP5	BCC-AVIM2.0 in CMIP6
♦ Soil-Vegetation-Atmosphere Transfer module	♦ Modified freeze-thaw scheme for soil water (below 0 degree and dependent on soil & water) (Xia et al., 2011)
♦ Multi-layer snow-soil scheme (same as NCAR CLM3)	♦ Improved parameterization of snow surface albedo (Chen et al., 2014) and snow cover fraction (Wu and Wu, 2004)
♦ Snow Cover Fraction scheme (sub-grid topography)	♦ Four-stream radiation transfer through vegetation canopy (Zhou et al., 2018)
♦ Vegetation growth module	♦ A vegetation phenology similar to Canadian Terrestrial Ecosystem Model (Arora and Boer, 2005)
♦ Soil carbon decomposition module	♦ Parameterized rice paddy scheme
♦ Land use change module (variable crop planting area)	♦ land VOC module (Guenther et al., 2012)

Table 4. Energy balance and cloud radiative forcing at the top-of-atmosphere (TOA) in the model with contrast to CERES/EBAF and CERES observations. Units:  $W \cdot m^{-2}$ .

	BCC-CSM2-MR (CMIP6)	BCC-CSM1.1m (CMIP5)	CERES/EBAF (OBS)	CERES (OBS)
Net energy at TOA	0.85	0.98	0.81	5.73
TOA outgoing longwave radiative flux	239.15	236.10	239.72	238.95
TOA incoming shortwave Radiation	340.46	341.70	340.18	341.47
TOA net shortwave radiative flux	239.09	235.96	240.53	244.68
TOA outgoing longwave radiative flux in clear sky	265.02	265.58	265.80	266.87
TOA net shortwave radiative flux in clear sky	288.67	288.71	287.68	294.69
Shortwave cloud radiative forcing	-49.55	-52.71	-47.16	-48.58
Longwave cloud radiative forcing	25.87	29.48	26.07	27.19

Notes: The model data are the mean of 1986 to 2005, while the available observation data are for 2003–2014.

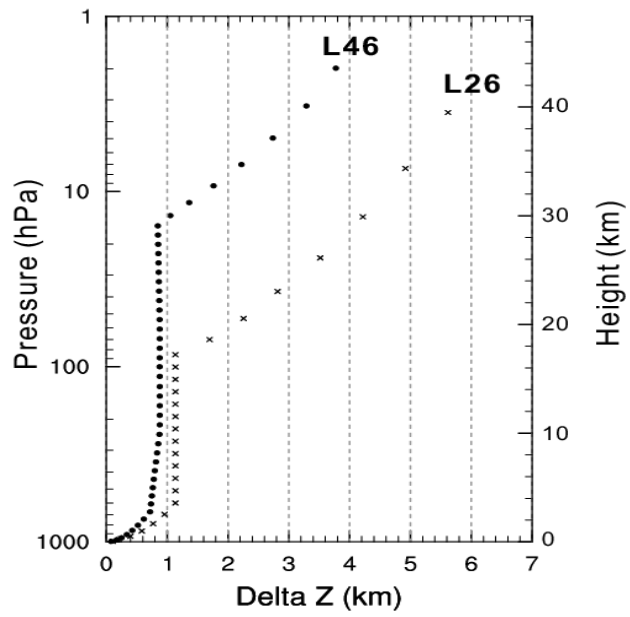
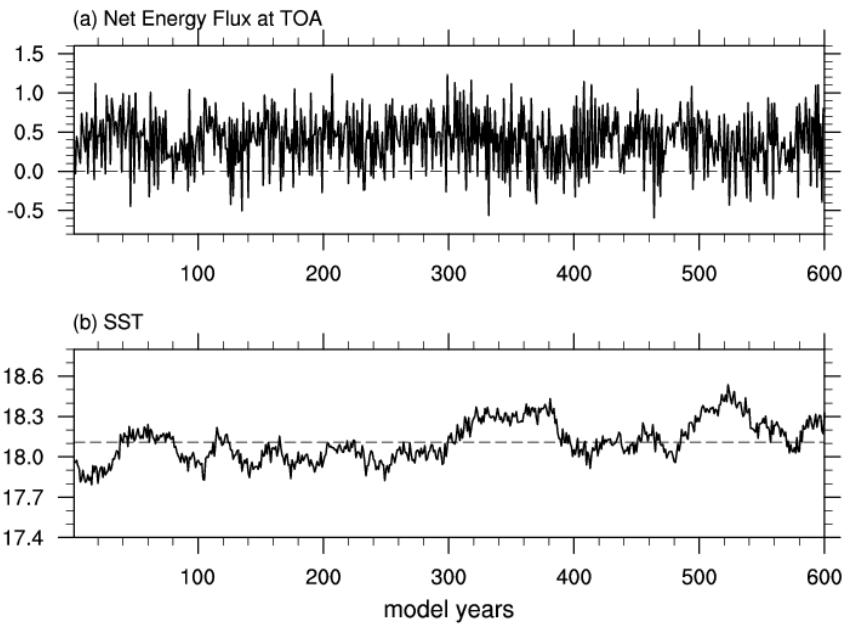


Figure 1. The profiles of layer thickness against the height for 26 vertical layers of the atmosphere in BCC-CSM-1.1m and 46 vertical layers in BCC-CSM2-MR.





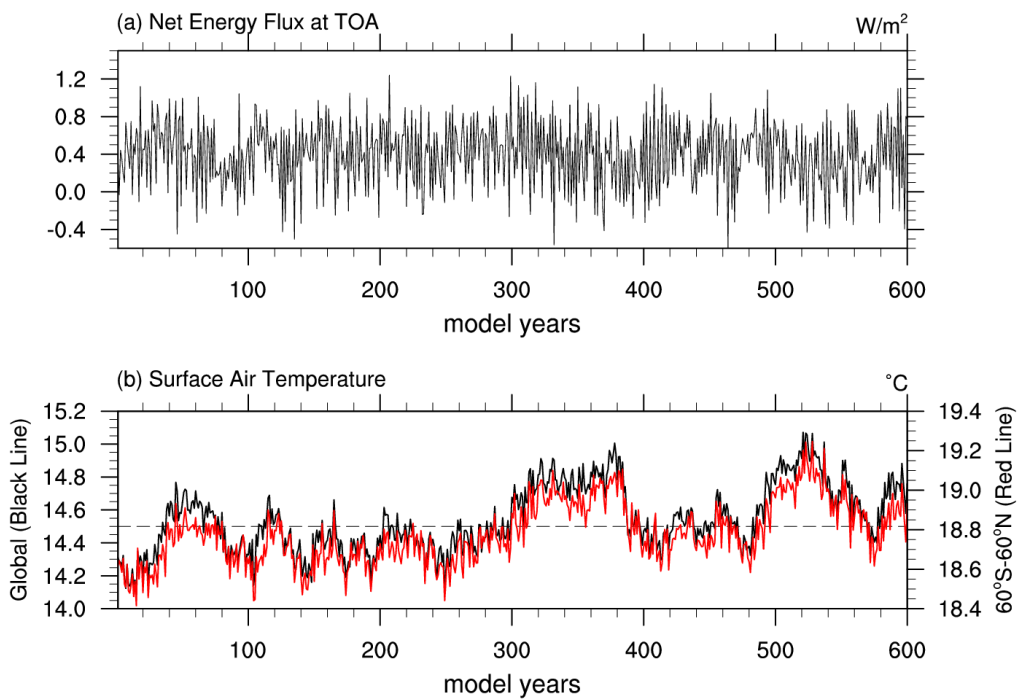


Figure 2. The time series of (a) global mean net energy flux at top of the atmosphere ( $\text{W m}^{-2}$ ) and (b) global (black line) and regional (60°S to 60°N, red line) surface air-sea surface temperature ( $^{\circ}\text{C}$ ) for the 600 years of piControl simulations.

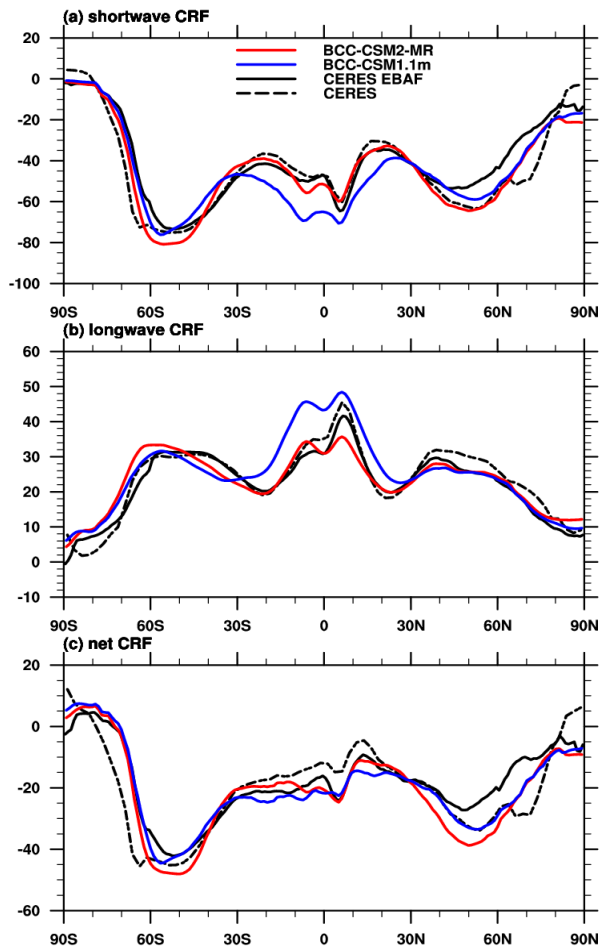


Figure 3. Zonal averages of the cloud radiative forcing from the BCC CMIP5 and CMIP6 models and observations (in  $\text{W m}^{-2}$ ; top row: shortwave effect; middle row: longwave effect; bottom row: net effect). Model results are for the period 1986–2005, while the available CERES ES-4 and CERES EBAF 2.6 data set are for 2003–2014.

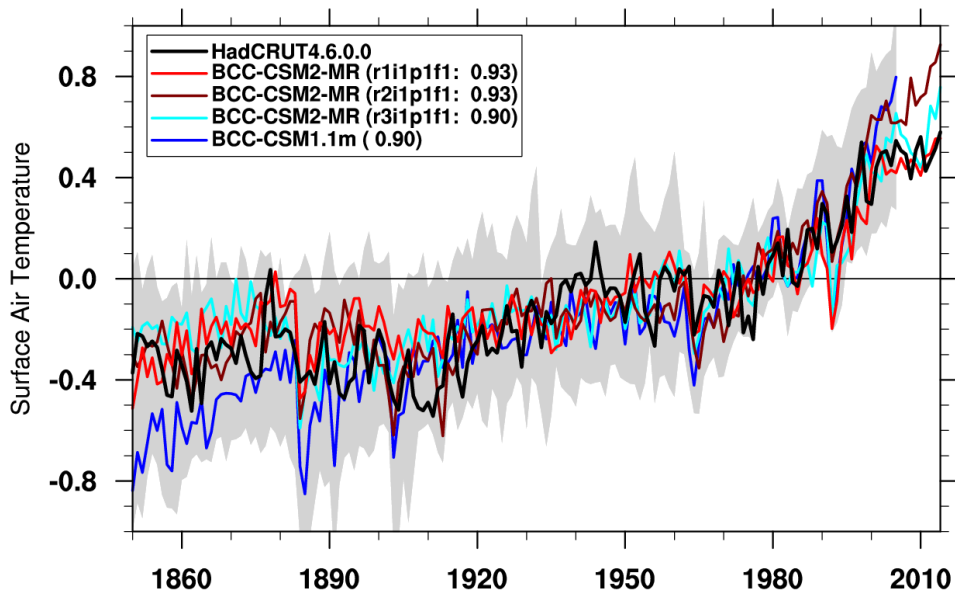


Figure 4. Time series of anomalies in the global (60°S to 60°N) mean surface air temperature from 1850 to 2014. The reference climate to deduce anomalies is for each individual curve from 1961 to 1990. Three lines labeled BCC-CSM2-MR denote three members of historical simulations from different initial state of the piControl simulation. The numbers in the bracket denote the correlation coefficient of 11-year smoothed BCC model data with the HadCRUT4.6.0.0 (Morice et al., 2012) observation. Gray shaded area shows the spread of 36 CMIP5 models data.

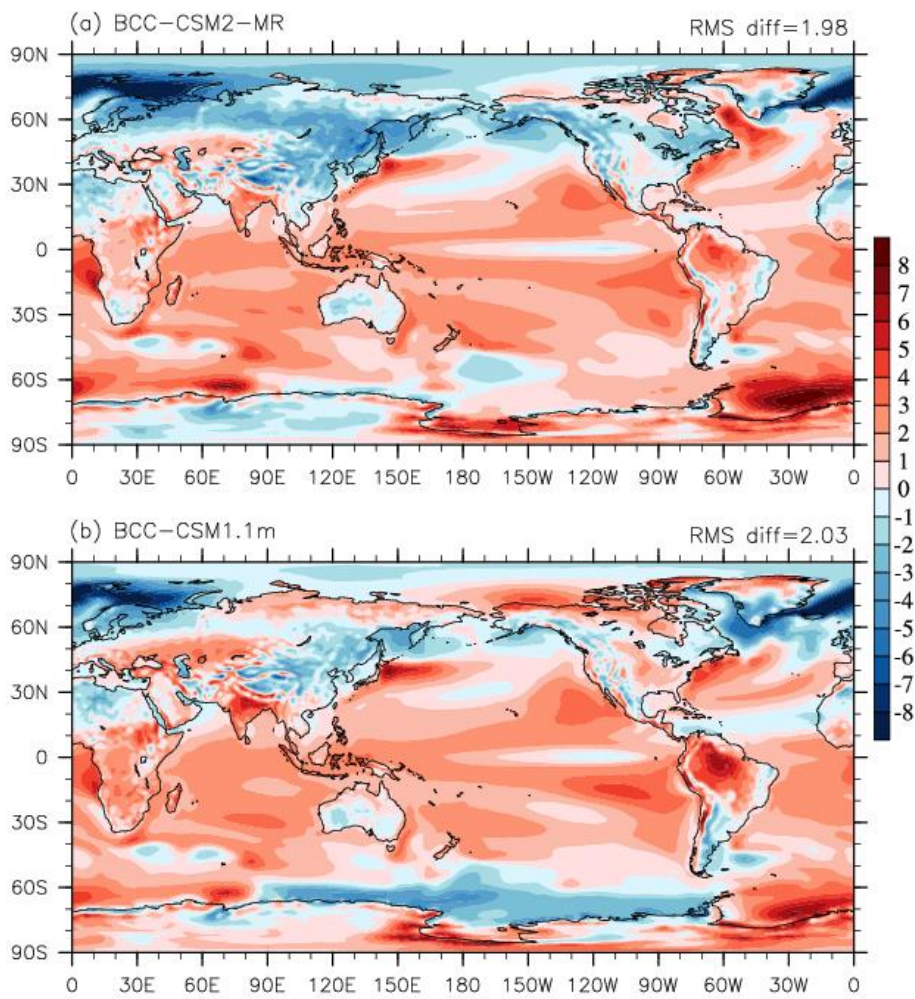


Figure 5. Annual-mean surface (2 meter) air temperature biases ( $^{\circ}\text{C}$ ) of (a) BCC-CSM2-MR and (b) BCC-CSM1.1m simulations with contrast to the reanalysis ERA-Interim for the period of 1986 to 2005.

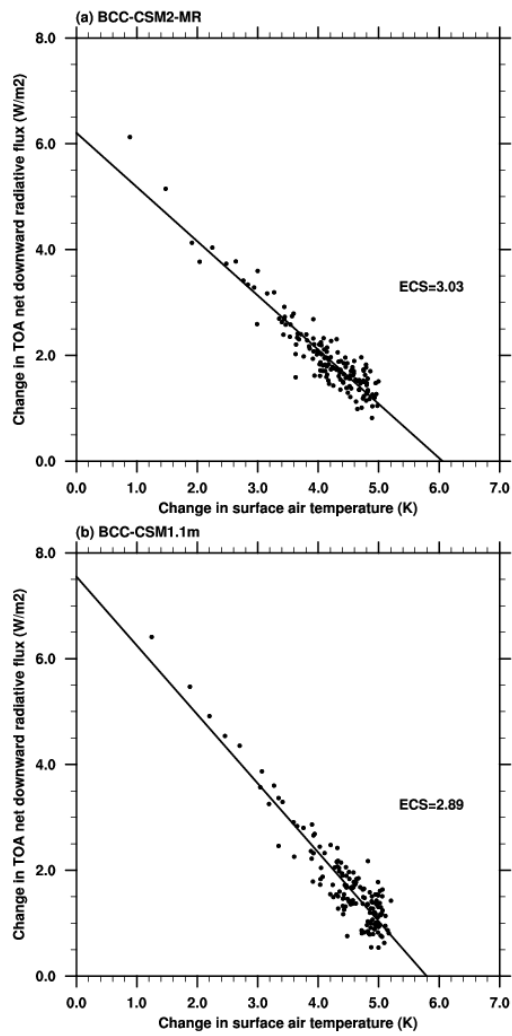


Figure 6. Relationships between the change in net top-of-atmosphere radiative flux and global-mean surface air temperature change simulated with an abrupt 4xCO<sub>2</sub> increase relative to the pre-industrial control run.

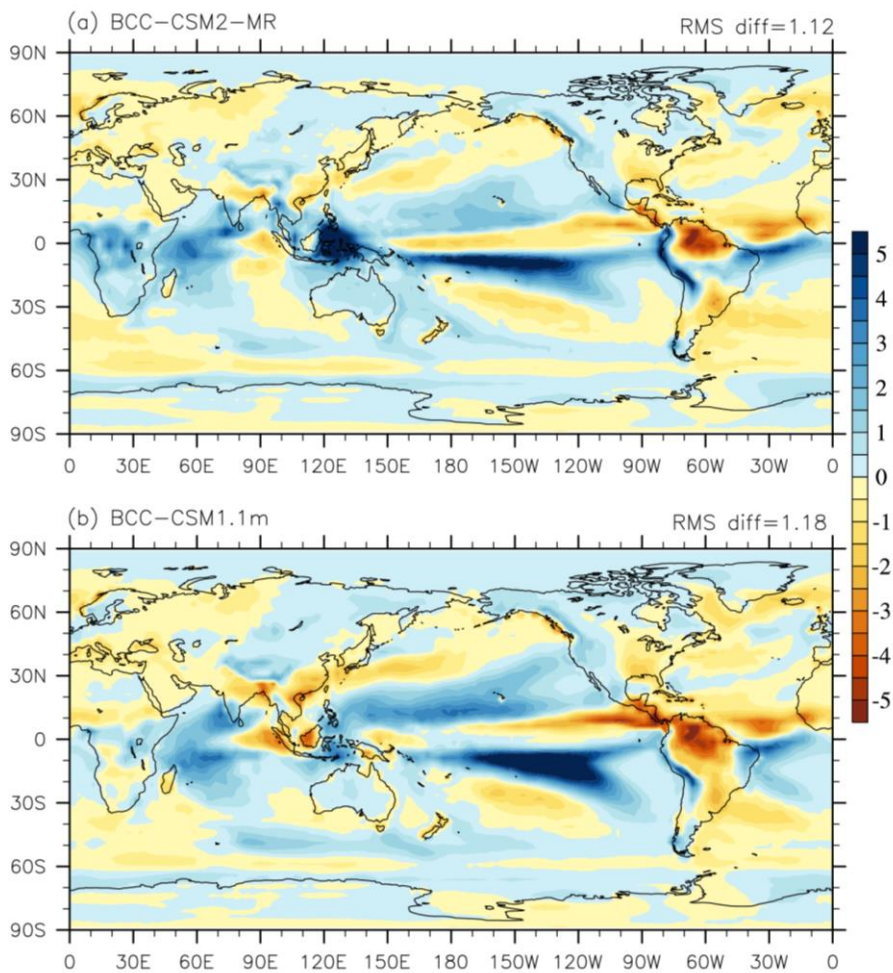


Figure 7. Annual-mean precipitation rate biases ( $\text{mm day}^{-1}$ ) of (a) BCC-CSM2-MR and (b) BCC-CSM1.1m simulations with contrast to 1986-2005 precipitation analyses from the Global Precipitation Climatology Project (Adler et al., 2003)

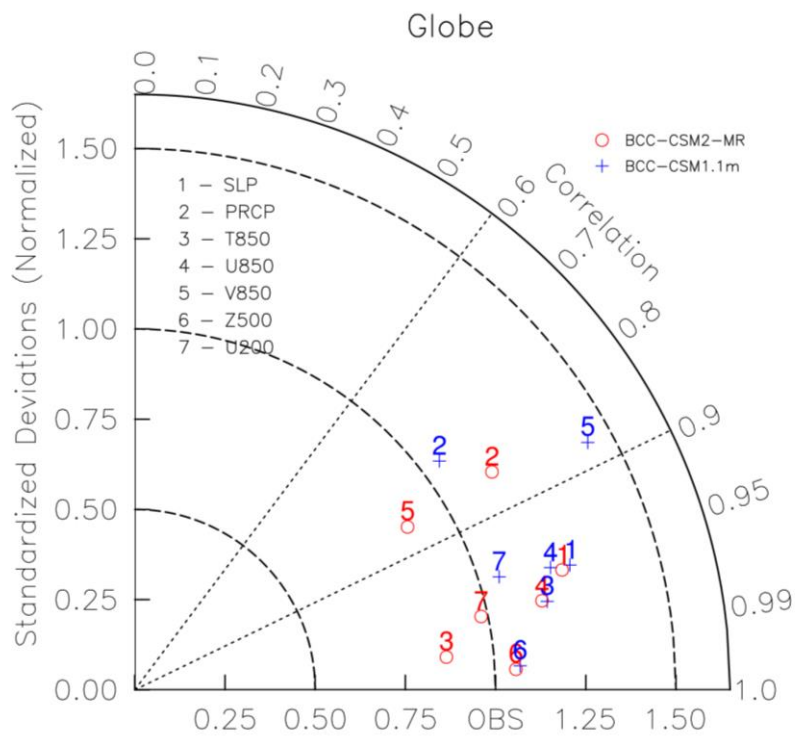


Figure 8. Taylor diagram for the global climatology (1980–2005) of sea level pressure (SLP), precipitation (PRCP), temperature at 850 hPa (T850), zonal wind at 850 hPa (U850), longitudinal wind at 850 hPa (V850), geopotential height at 500 hPa (Z500), and zonal wind at 200 hPa (U200). The radial coordinate shows the standard deviation of the spatial pattern, normalized by the observed standard deviation. The azimuthal variable shows the correlation of the modelled spatial pattern with the observed spatial pattern. Analysis is for the whole globe. The reference dataset is ERA-Interim except the precipitation from Global Precipitation Climatology Project dataset. The model results of BCC-CSM2-MR and BCC-CSM1.1m are the mean for 1980 to 2000. Blue crosses are for BCC-CSM1.1m and circles for BCC-CSM2-MR.

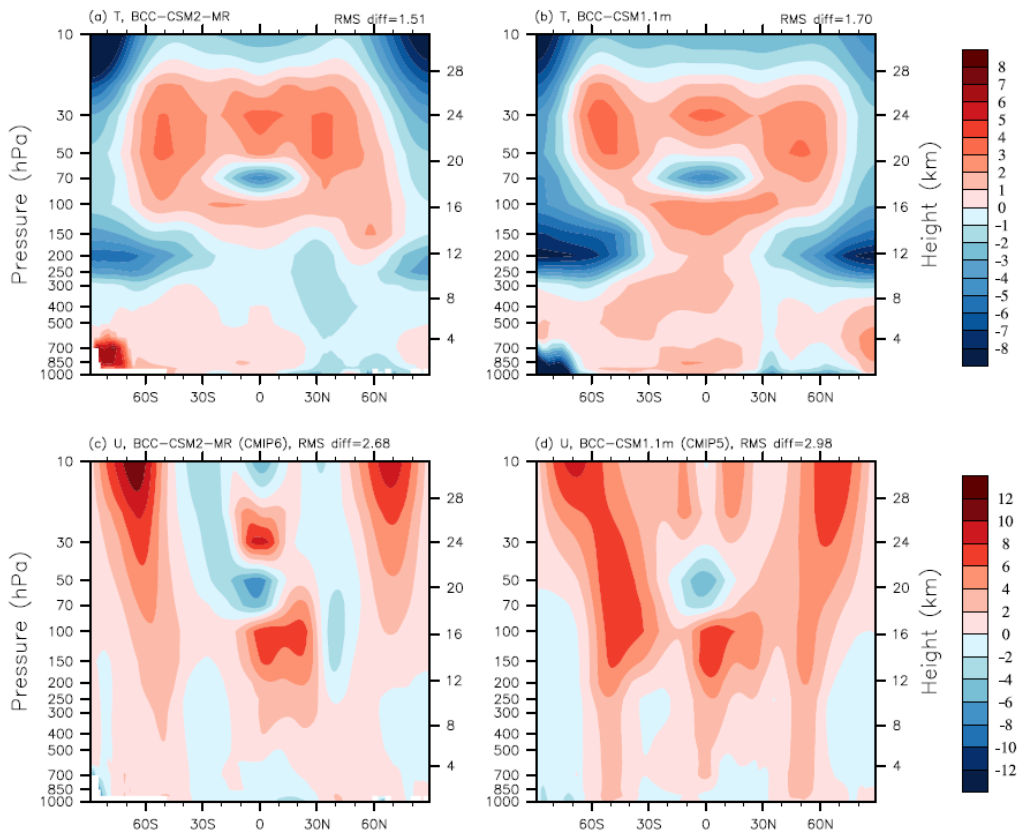


Figure 9. Pressure-latitude sections of annual mean temperature (top panels, K) and zonal wind (bottom, m s<sup>-1</sup>) biases for BCC-CSM2-MR (left) and BCC-CSM1.1m (right), with respect to the reanalysis ERA-Interim for the period of 1986 to 2005.

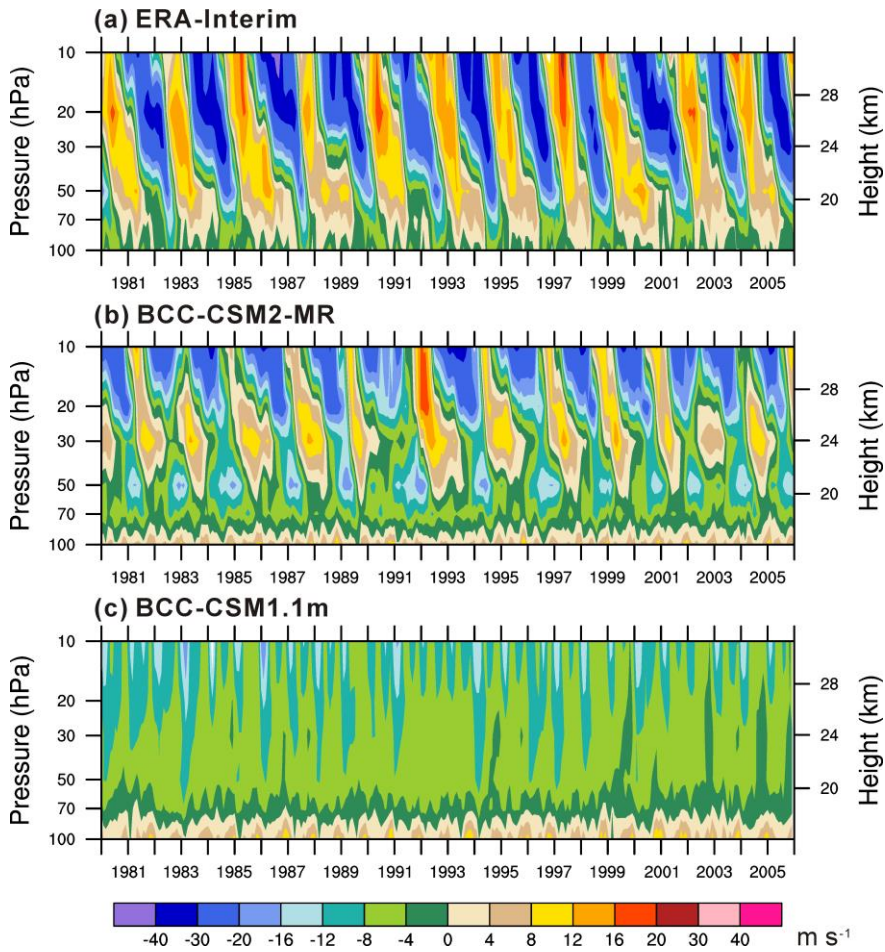


Figure 10. Tropical zonal winds ( $\text{m s}^{-1}$ ) between  $5^{\circ}\text{S}$  and  $5^{\circ}\text{N}$  in the lower stratosphere from 1980 to 2005 for (a) ERA-Interim reanalysis, (b) BCC-CSM2-MR, and (c) BCC-CSM1.1m.

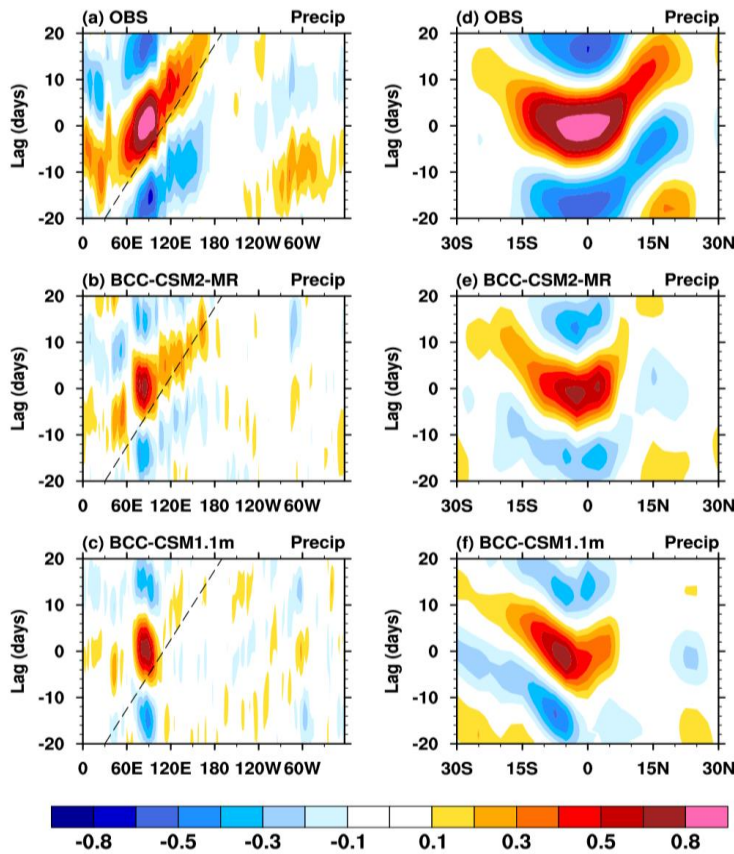


Figure 11. Left panels: longitude-time evolution of lagged correlation coefficient for the 20–100 day band-pass-filtered anomalous rainfall (averaged over 10°S–10°N) against itself averaged over the equatorial eastern Indian Ocean (75°E–85°E; 5°S–5°N). Right panels: same as in the left panels but to show meridional propagation of the filtered rainfalls, and lagged correlation coefficient for anomalous rainfall (averaged over 80°E–100°E) against the rainfall averaged over the same region of equatorial eastern Indian Ocean. Dashed lines in each panel denote the 5 m s<sup>-1</sup> eastward propagation speed. The reference GPCP observations and historical simulations of models are from the period of 1997–2005.

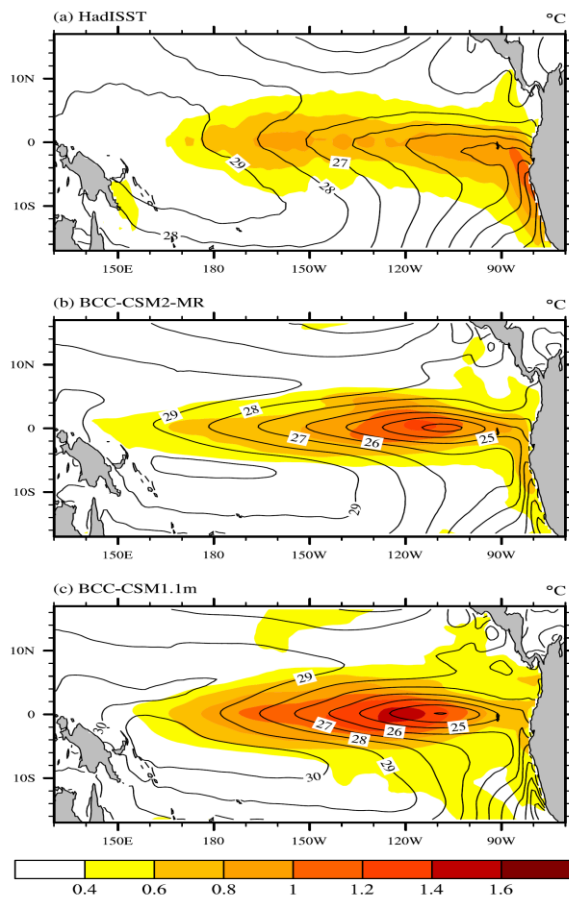


Figure 12. The spatial distributions of 1986-2005 annual mean sea surface temperature (contour lines, °C) and its standard deviation of interannual anomalies (shaded area, °C) in the tropical Pacific for (a) HadISST observations (Rayner et al., 2003), (b) BCC-CSM2-MR, (c) BCC-CSM1.1m.

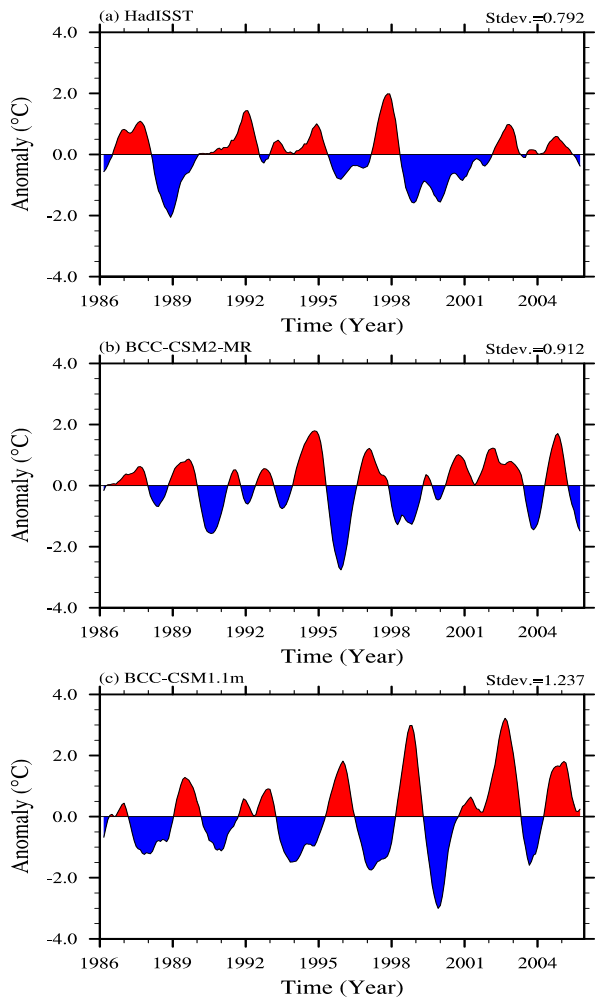


Figure 13. The time series of Niño3.4 SST Index from 1986 to 2005 for (a) HadISST data, (b) BCC-CSM2-MR, (c) BCC-CSM1.1m.

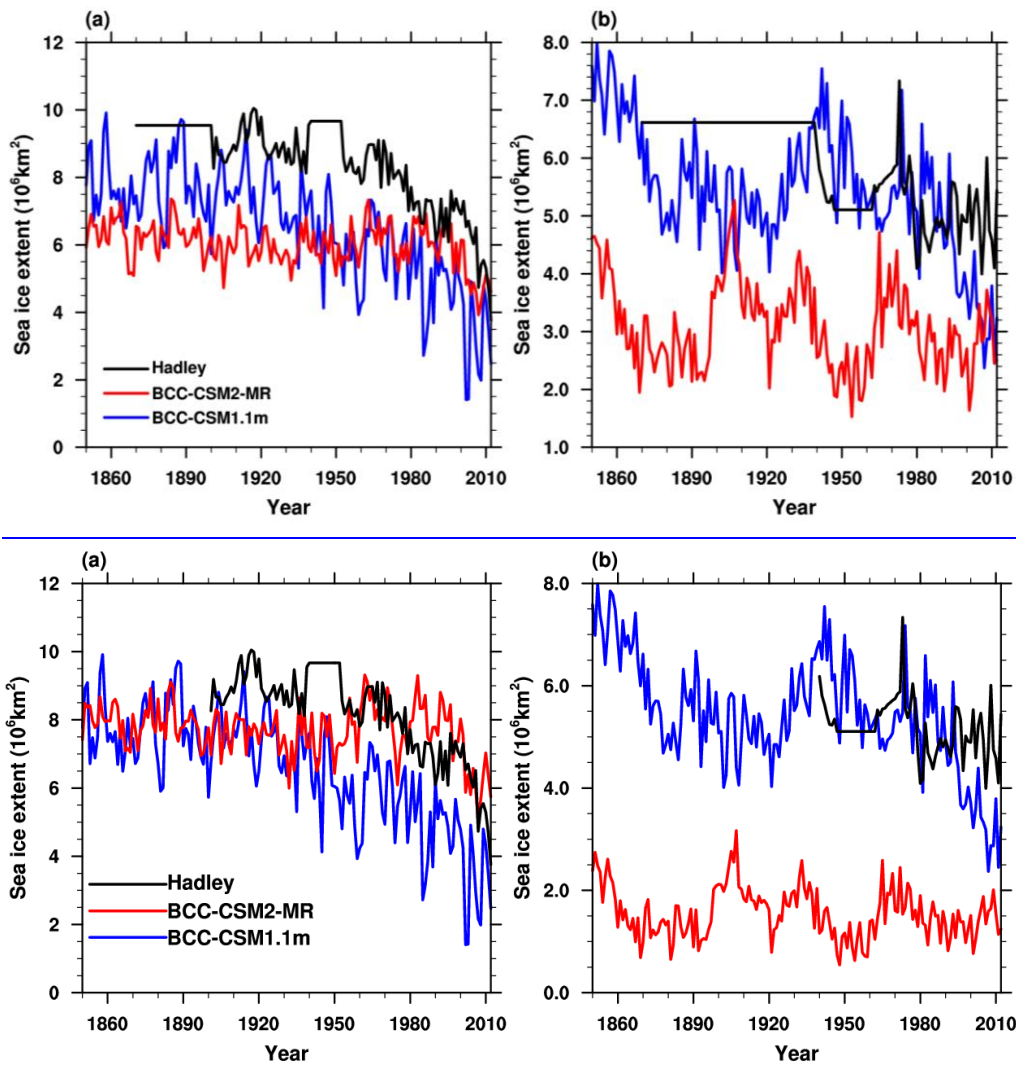
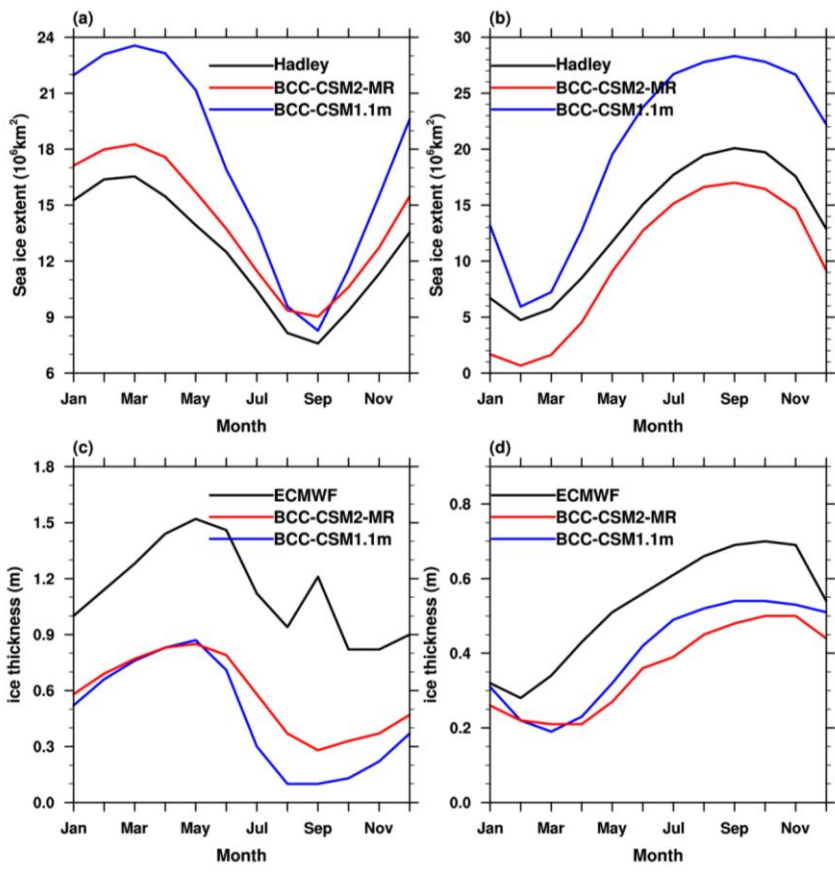


Figure 14. Time-series of sea-ice extent from 1851 to 2012 for (a) the Arctic in September and (b) the Antarctic in

March as simulated in BCC-CSM2-MR and BCC-CSM1.1m and observations that are derived from Hadley Centre Sea Ice and Sea Surface Temperature data set (Rayner et al., 2003).

| \_\_\_\_\_



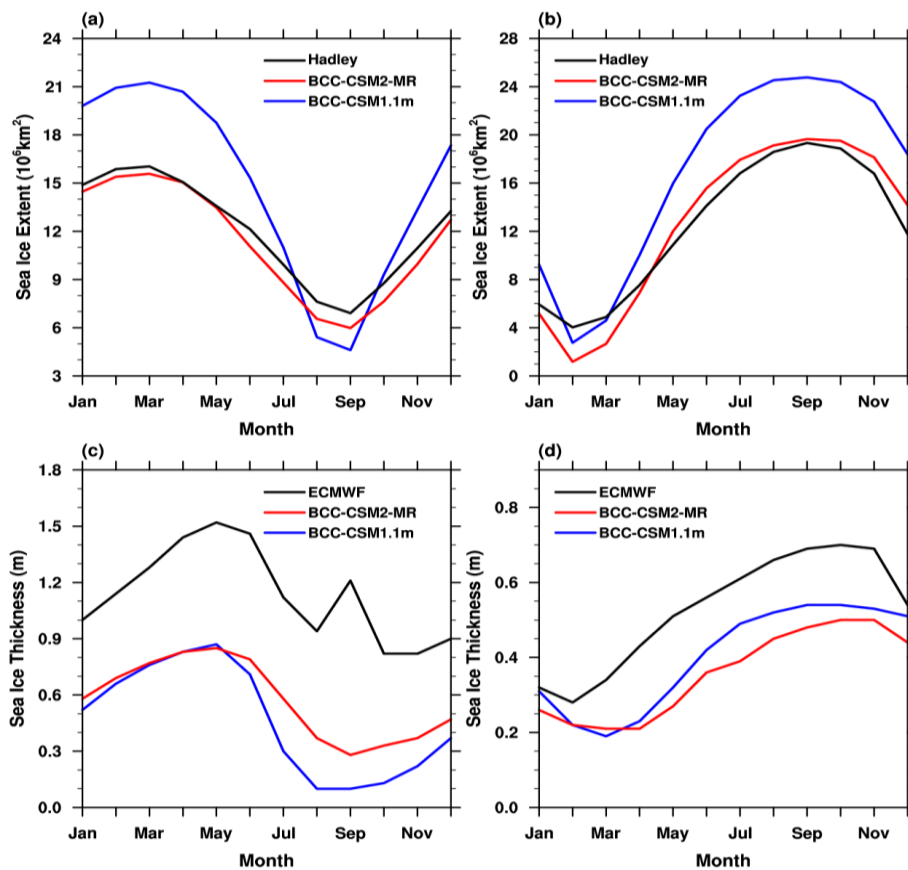


Figure 15. Mean (1980–2005) seasonal cycle of sea-ice extent (upper panel, the ocean area with a sea-ice concentration of at least 15%) and mean thickness (lower panel) in the Northern Hemisphere (left) and the Southern Hemisphere (right). The observed seasonal cycles of sea-ice extent in (a) and (b) are derived from 1980-2005 Hadley Centre Sea Ice and Sea Surface Temperature data set (Rayner et al., 2003), and the ice thickness in (c) and (d) are derived from 1980-2005 global gridded data set based on European Center for Medium-Range Weather Forecast (Tietsche, et al., 2014).

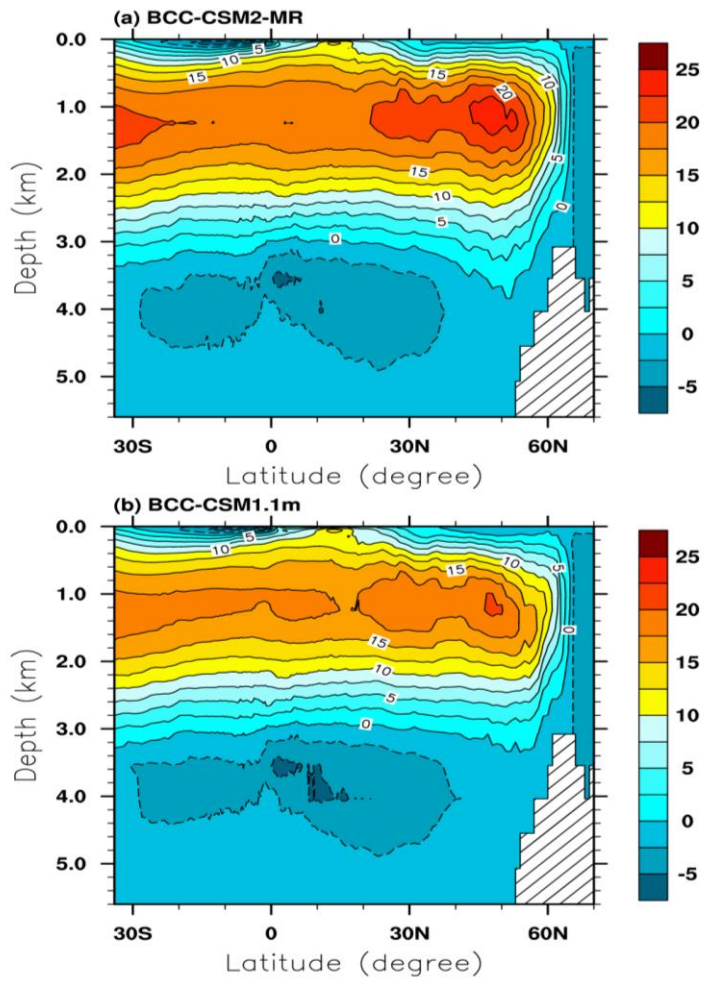


Figure 16. Zonally-averaged streamfunction of the Atlantic Meridional Overturning Circulation (AMOC) for the period of 1980 to 2005 in BCC-CSM2-MR (top) and BCC-CSM1.1m (bottom). Units: Sv

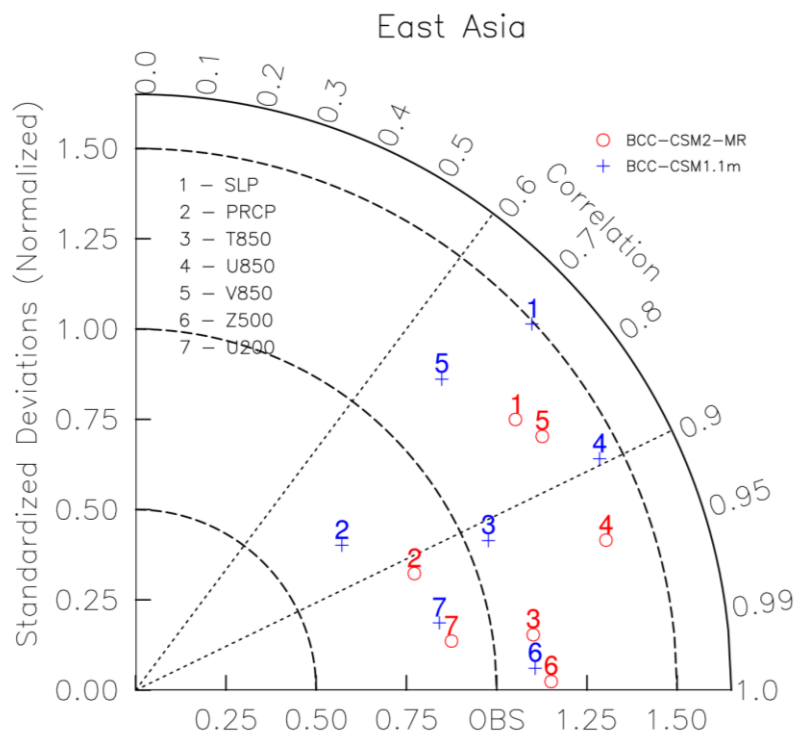
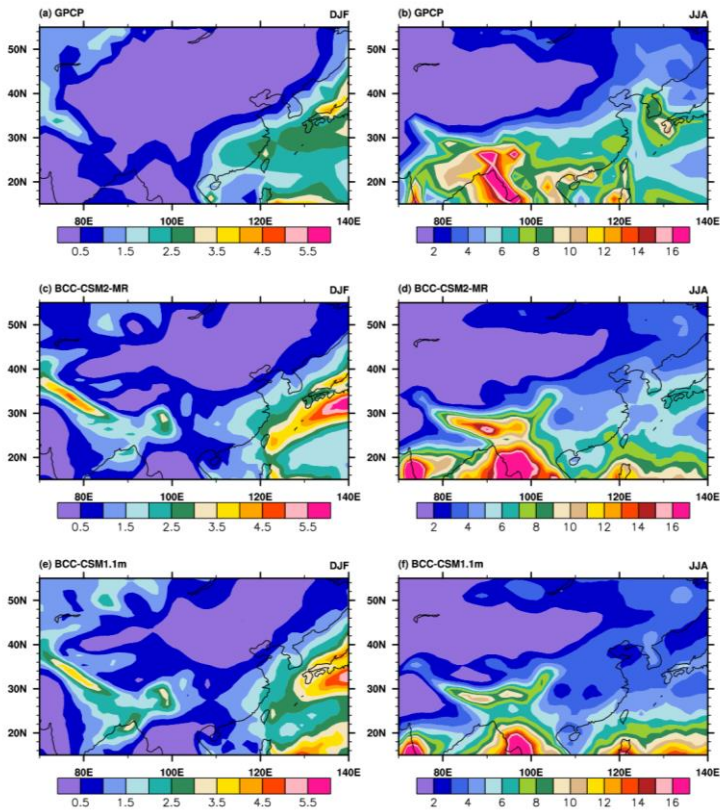


Figure 17. Same as in Figure 8, but for the domain covering East Asia (20°–50°N, 100°–140°E).



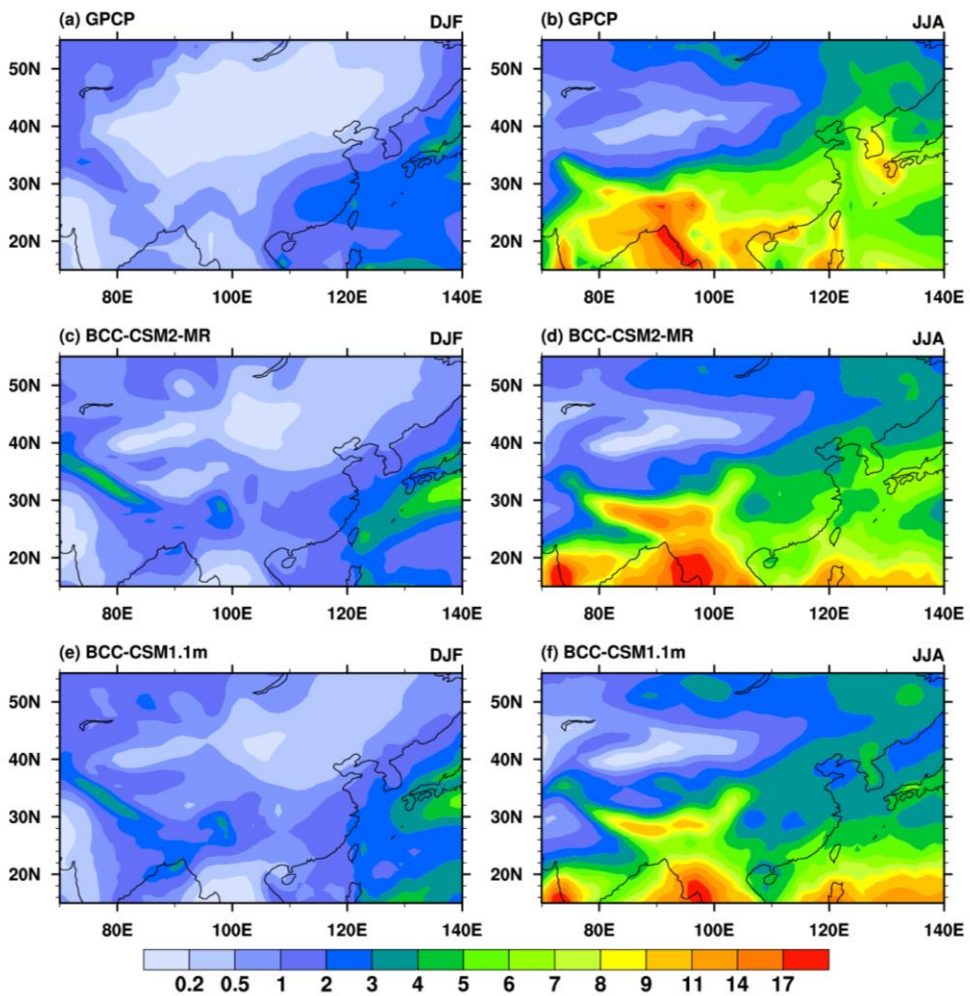


Figure 18. Regional distribution maps of precipitation climatology (averaged from 1980 to 2005) for December-January-February (left panels) and June-July-August (right panels) from (a) GPCP, (b) BCC-CSM2-MR, (c) BCC-CSM1.1m. Units:  $\text{mm day}^{-1}$ .

带格式的: 上标

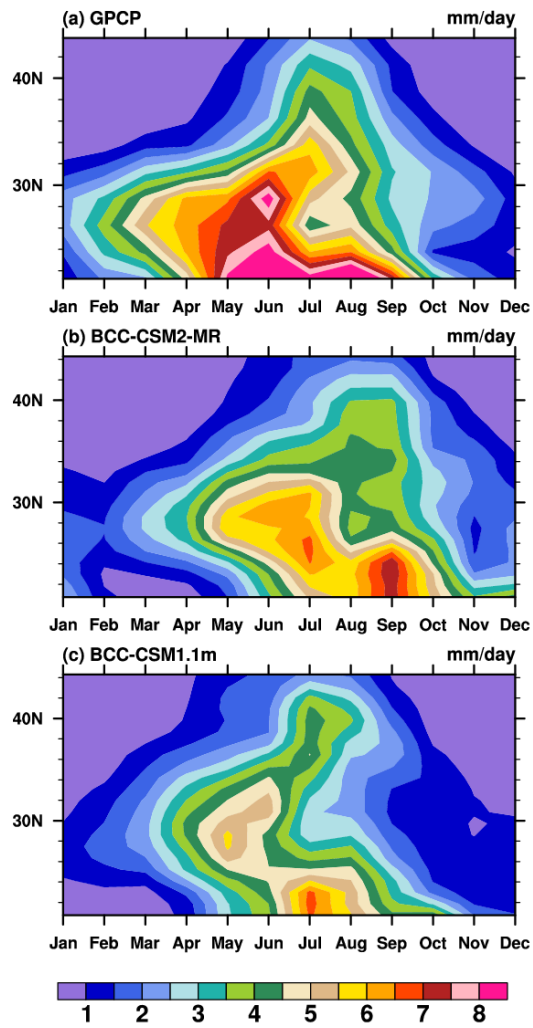


Figure 19. Latitude (from 20°N to 25°N) – month (Jan. to Dec.) diagrams showing variations of monthly precipitation averaged over 100°E–120°E and for the period of 1980–2005. (a) GPCP, (b) BCC-CSM2-MR, (c) BCC-CSM1.1m. Units: mm day<sup>-1</sup>.

带格式的: 上标

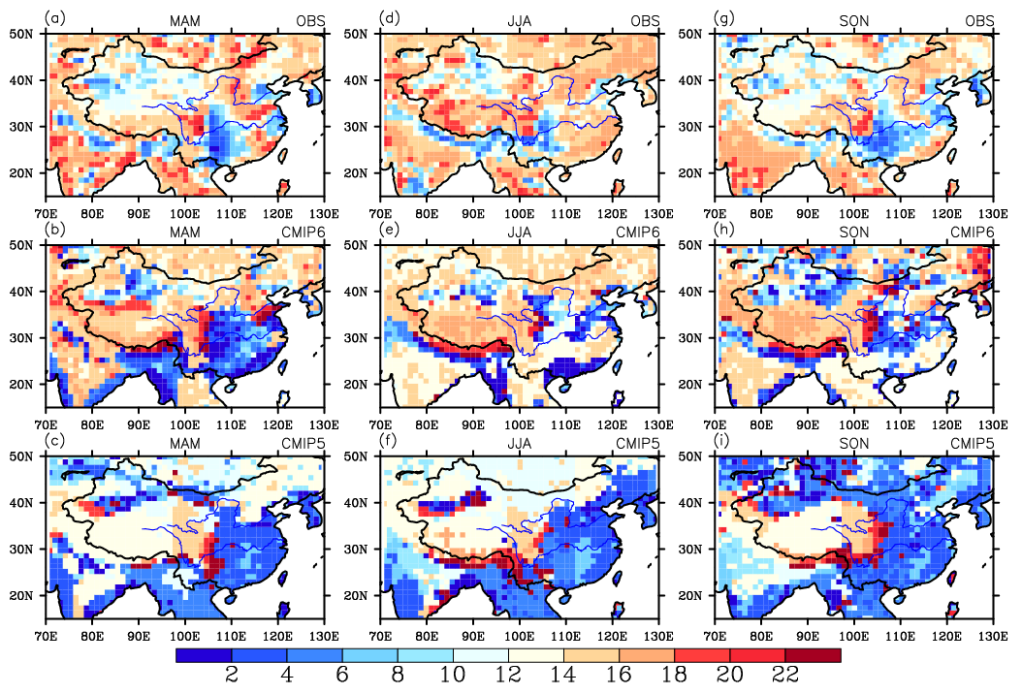


Figure 20. Local times of maximum frequency of rainfall occurrence in March-April-May (left column), June-July-August (middle column), and September-October-November (right column) over China and its surrounding areas for BCC-CSM2-MR (middle panel), BCC-CSM1.1m (bottom panel), and TRMM data (top panel, Huffman et al., 2014). The rainfall occurrence is defined as the hourly precipitation larger than 1 mm.